JOURNAL OF GEOPHYSICAL RESEARCH, VOL. 104, NO. E10, PAGES 24,075–24,094, OCTOBER 25, 1999

Circular-polarization radar properties of high-altitude ice: Western Kunlun Shan and central Andes

Albert F. C. Haldemann[1] and Duane O. Muhleman

Division of Geological Sciences, California Institute of Technology, Pasadena, California

Abstract. Full polarization synthetic aperture radar images of high-altitude glaciers and ice fields in the Western Kunlun Shan of Tibet and the central Andes near Santiago, Chile, made with the shuttle imaging radar, display regions with circular-polarization ratios, μ_c, in excess of unity. The mountainous topography at both locales allows reconstruction of the angular scattering behavior. The behavior is very similar to that displayed by Greenland's percolation zone. Glaciologic evidence from the Tibetan site confirms ice pipes and lenses embedded in the firn, which have been identified as the scatterers producing $\mu_c>1$ in Greenland. This demonstrates that the cold snow percolation facies radar signature exists outside of Greenland. The Greenland radar behavior had been suggested as an analogue for that of the icy Galilean satellites. We, like previous workers, find that the near-nadir backscatter is too specular to be considered analogous to that of the Jovian moons. We also present a crevasse region in Tibet that exhibits $\mu_c>1$ and a possible detection of the ice substrate of a rock-covered glacier in the Andes.

1. Introduction

Two Space Radar Lab missions of the Space Shuttle Endeavor (SRL-1 and SRL-2) flown in April and October of 1994 carrying the Shuttle Imaging Radar / X-band Synthetic Aperture Radar (SIR-C/X-SAR) instrument payload obtained some full polarization, multi-frequency information. These data offer an opportunity to synthesize circular polarization results over a variety of terrestrial terrains. Terrestrial circular-polarization data can be more directly compared with planetary radar observations which typically employ circular polarizations. Specifically, we address the topic of circular-polarization radar scattering by terrestrial ices and compare the behavior to planetary ice radar scattering. This work extends the circular-polarization observations of ice radar scattering in Greenland [*Rignot et al.*, 1993] to high elevations at temperate latitudes.

1.1. Planetary Ice Radar Scattering

Planetary ices display unique radar scattering properties that distinguish them from rocky planetary surfaces. This is shown schematically in Figure 1. This behavior, first described for the Galilean satellites by *Campbell et al.* [1977], consists of high backscatter cross section, σ°, and circular-polarization ratio inversion relative to terrestrial planets. The σ° enhancement is significant at all incidence angles, and in particular, the echo in the same sense of circular-polarization as transmitted (SC) is greater than the echo in the opposite sense (OC). Thus the ratio of these quantities, or circular-polarization ratio, μ_c=SC/OC>1. A value of μ_c=1 is produced, for example, by a volume distribution of randomly oriented dipole scatterers, whereas a distribution of randomly oriented dipoles on a surface produces μ_c<1, typical of rocky planetary observations. *Ostro* [1982] and *Ostro et al.* [1992] review all observations confirming similar behavior for each of the icy Galilean satellites, Europa, Ganymede, and Callisto (EGC). The angular dependence of EGC backscatter is very different from that of terrestrial planets: where the latter exhibit a strong glint in the subradar region and a subdued diffuse scatter elsewhere, EGC behavior consists of a strong Lambertian-like scattering over the whole disk ($\sigma^\circ \sim \cos^n(\theta_i)$, with n~1.5, where θ_i is the incidence angle). The behavior appears to be characteristic of cold icy surfaces and is also observed at Mars' residual south polar cap [*Muhleman et al.*, 1991] and in permanently shadowed craters on Mercury [*Slade et al.*, 1992; *Harmon and Slade*, 1992; *Harmon et al.*, 1994], where thermal models [*Butler* 1994; *Butler et al.*, 1993; *Paige et al.*, 1992] indicate ice is stable.

Pure surface scattering models are unable to describe the effect, and cold ice is highly transparent to radar wavelengths, so a volume-scattering explanation is appropriate. At least five different theoretical models have been suggested to explain EGC radar behavior [*Ostro and Pettengill*, 1978; *Goldstein and Green*, 1980; *Ostro*, 1982; *Hagfors*, 1985; *Hapke*, 1990; *Hapke and Blewitt*, 1991; *Eshleman*, 1986; *Gurrola*, 1995]. Most recent analyses [*Ostro et al.*, 1992] imply some coherent backscatter [*Hapke*, 1990; *Hapke and Blewitt*, 1991; *Peters*, 1992], which produces μ_c<2. Coherent backscatter consists of a sequence of multiple forward scattering events that preserve the helicity of the incident circularly-polarized radar signal while redirecting it into the backscatter direction. Both directions along a scattering pathway are followed, leading to a coherent addition of the signal in the backscatter direction, producing the observed, enhanced cross sections.

[1]Now at Jet Propulsion Laboratory, Pasadena, California.

Paper number 1999JE900023.
0148-0227/99/1999JE900023$09.00

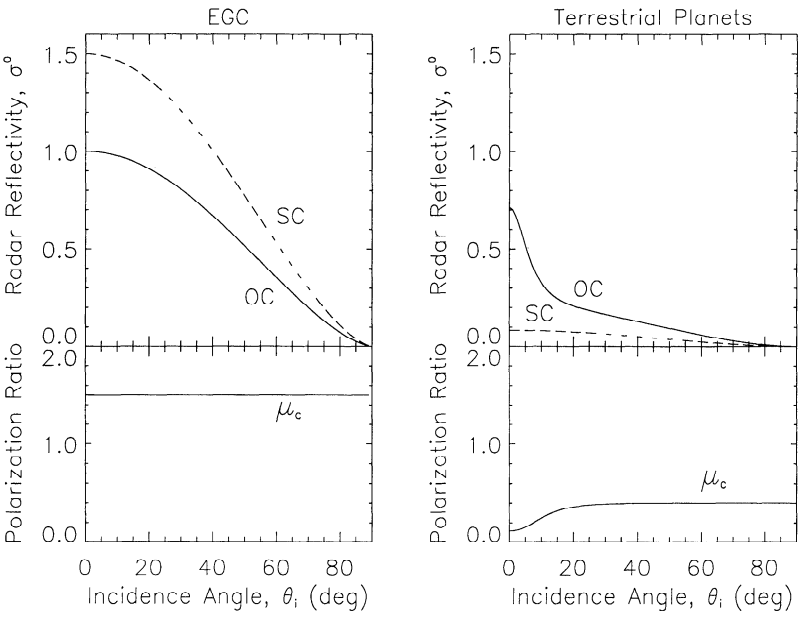

Figure 1. Schematic comparison of the typical backscatter dependence on incidence angle for a terrestrial planet with that of the icy Galilean satellites, Europa, Ganymede, and Calisto (EGC). The θ_i is incidence angle. Radar reflectivity scale is approximate only.

1.2. Terrestrial Ice Radar Scattering

The radar behavior of ices on Earth, in contrast to the planetary examples, depends critically on the presence of liquid water, which with its high dielectric constant, strongly controls the scattering process. The liquid water content, in turn, depends on the terrestrial glaciologic and hydrologic processes that act within Earth's cryosphere. On glaciers and ice fields the equilibrium line divides the accumulation zone from the ablation zone. There is annual net gain of mass above the equilibrium line, and net loss below. Following *Benson* [1962] and *Paterson* [1994], the accumulation zone is divided from the head of the glacier toward the equilibrium line into the dry-snow zone, the percolation zone, the wet-snow zone, and the superimposed-ice zone, shown in Figure 2. Depending on local climate, the dry-snow zone and percolation zone may be missing on some glaciers or ice fields.

The different zones can be distinguised by radar remote sensing [*Ulaby,* 1982; *Ulaby et al.,* 1984]. Wet snow is relatively radar-dark (low backscatter cross section, σ°): the flat, high dielectric-contrast surface tends to reflect the radar in the forward direction. The dry-snow zone also exhibits low backscatter due to penetration into firn without scatterers and due to the generally flat surface. When wet, the percolation zone behaves similarly to wet snow. When it is cold and dry, however, it exhibits high σ°, due to volume scattering from the buried ice structures. Exposed ice can also have high σ° due apparently to a roughened surface and perhaps also to its cracked interior. Thus it is apparent that the interpretation of radar images of terrestrial ice fields and glaciers requires some amount of contextual information. *Bindschadler and Vornberger* [1992] detected the snow line in Seasat synthetic aperture radar (SAR) imagery of Greenland and also noted high backscatter from bare ice regions corresponding to crevasse zones. The Seasat observations [*Bindschadler et al.,* 1987; *Bindschadler and Vornberger,* 1992] spurred SAR observations of Greenland by demonstrating that the different snow zones could be distinguished and monitored. *Forster et al.* [1996] used SIR-C data to examine the South Patagonian Icefield (SPI), and *Albright et al.* [1998] studied the Mount Everest region. Both successfully classified the various ice

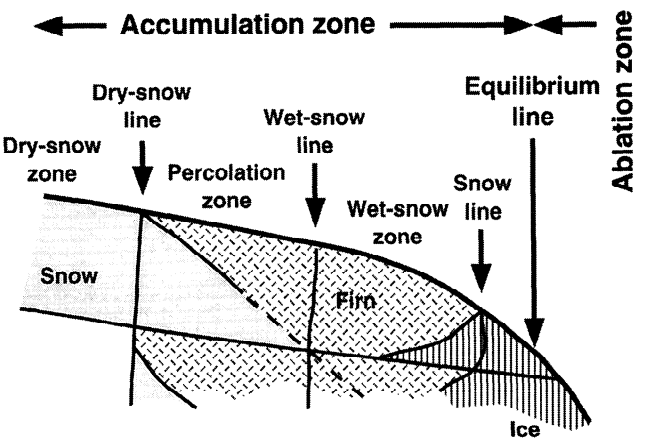

Figure 2. Glacier and ice field zonation [from *Paterson,* 1994, reprinted by permission of Butterworth Heinemann Publishers, a division of Reed Educational and Professional Publishing Ltd.; *Benson,* 1962]. No melting takes place in the dry-snow zone, even in summer. In the percolation zone some melting occurs. The water percolates downward, where it may encounter a hydrologic discontinuity and spread out before refreezing. In refreezing, ice layers or lenses form, and the vertical percolation channels refreeze as ice pipes or glands. Proceeding downglacier, the wet-snow line is eventually reached, where the whole year's snow reaches melting temperature in the wet-snow zone. In this zone some meltwater percolates into previous years' deeper layers. The zone where the meltwater produces a continuous mass of ice on refreezing is the superimposed-ice zone. The boundary between the wet-snow zone and the superimposed-ice zone is the snow line.

and snow zones based on linear-polarization data only. *Benson et al.* [1996] made similar observations with single linear-polarization ERS-1 SAR measurements in Alaska. *Rott and Davis* [1993] made multifrequency and polarimetric studies of alpine glacier radar behavior with the Jet Propulsion Laboratory's (JPL's) Airborne SAR (AIRSAR) in view of glacier snow-ice classification, but without specifically isolating circular-polarization behavior. They did observe that crevasses scatter like trihedral corner reflectors.

In 1991, the AIRSAR was flown over Greenland, and circular-polarizations were synthesized from the data. *Rignot et al.* [1993] discovered that the percolation zone exhibits radar properties somewhat resembling those of planetary ices, in particular, at 5.6 and 24 cm. The general behavior of the *Rignot et al.* [1993] Greenland AIRSAR measurements is plotted as a function of incidence angle θ_i in Figure 3. A comparison of Figures 1 and 3 shows that the details of the Greenland radar properties are quite different from those of EGC. *Rignot et al.* [1993] point this out firmly. Whereas the percolation zone properties averaged over θ_i are similar to disk-averaged EGC properties, the 24 cm Greenland normalized radar cross section σ° is much lower than the 5.6 cm σ°, and 68 cm P-band does not present the EGC signature at all. EGC radar properties, on the other hand, are apparently maintained from 3.5 cm out as far as 70 cm. Furthermore EGC μ_c exceeds unity at all incidence angles, while the percolation zone only exhibits the behavior at $\theta_i \geq 30^\circ$. The linear-polarization ratio μ_l=HV/HH was also examined by *Rignot et al.* [1993]. The values are greater than the μ_l=1/3 expected for volume distributions of random dipole scatterers. Various lines of evidence including emissivity models of ice inclusions [*Zwally*, 1977], and surface-based radar observations [*Jezek et al.*, 1994] point to the refrozen ice inclusions in the firn as responsible for the percolation zone radar behavior. *Rignot* [1995] developed a fairly successful single-scattering model for the ice pipes and lenses that produces the large radar reflectivities and polarization ratios by internal reflections within the icy inclusions. The percolation zone scattering manifestly requires liquid water, which seems unlikely on other planetary bodies. So the Greenland result is exciting and provides an important analogy for EGC; however, it is not a complete analogy, as it does not address the EGC behavior at small incidence angle [*Rignot*, 1995].

The goal of the present study is to expand the search for unique radar scattering behavior by terrestrial ice deposits. With this effort, we address three questions. (1) How widespread is the Greenland ice scattering behavior on Earth? (2) Do planetary analogue ice scattering behaviors exist in other terrestrial ice morphologies? (3) Can these ice scattering observations contribute to further terrestrial and planetary remote sensing?

2. SIR-C High-Altitude Observations

To expand on the Greenland AIRSAR precedent, we examine the circular-polarization radar behavior of ices elsewhere on Earth. The SIR-C instrument offers a data set that covers the globe. On SRL-1, 207 full-polarization tracks were planned, while for SRL-2, the number was 211. SIR-C coverage, however, was limited to +/-57° latitude.

There are nonpolar locations on Earth where, for a large part of the year, all the water on an ice field is frozen, and what remain are snow, firn, and ice structures. Some such locations are at midlatitude at high elevation. The tropospheric temperature lapse rate around 6°km^{-1} [*Holton*, 1992] takes a mean sea level surface air temperature of 20°C to below -4°C above 4000 m. An annual mean sea level surface air temperature of 20°C or colder is found at latitudes north and south of about 30° [*Peixoto and Oort*, 1992]. *Benson* [1962]

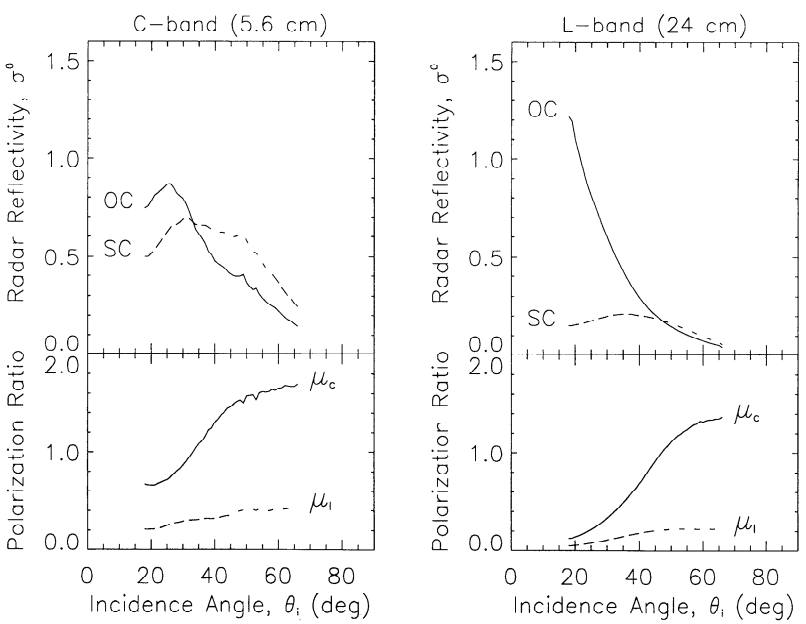

Figure 3. AIRSAR-observed circular-polarization radar behavior of the Greenland ice cap percolation zone as a function of incidence angle θ_i at both C-band and L-band wavelengths; data from *Rignot* [1995]. OC refers to opposite sense of circular-polarization received to that transmitted, and SC refers to same sense circular-polarization received. Specifically the circular-polarization ratio is $\mu_c = \sigma^\circ(RR) / \sigma^\circ(RL)$. Linear-polarization ratio is $\mu_l = \sigma^\circ(HV) / \sigma^\circ(HH)$. R, L, H and V refer to right, left, horizonal, and vertical polarizations, respectively.

carried out similar extrapolations to define the mean annual temperatures on Greenland corresponding to the borders between the various snow zones: the dry-snow line always lies above (in elevation) a mean annual isotherm of T=-25°C, while the snow line lies around $\overline{T}$=-10°C. *Benson* [1962] points out that the important temperature for mapping zone boundaries is not the air temperature so much as the ice temperature and, specifically, the depth of the melting isotherm, which depends very much on the temperature history during the melting season. Thus, while dry-snow conditions at 30°N seem unlikely because there are no 8000 m peaks, local microclimates and sun-shadowing might produce locally favorable conditions for a percolation zone at 5000 m or below.

A high-altitude criterion was applied, reducing the set of SIR-C full-polarization tracks of interest to 19 from SRL-1 and 27 from SRL-2 [*Haldemann,* 1997]. Two locations were chosen for further study, one data take (DT) from SRL-1 (DT 1/58.10: Kunlun Mountains, Tibet), and one from SRL-2 (DT 2/40.60: central Andes Mountains). Both are springtime scenes in their respective hemispheres, when we hoped the firn would still be in a frozen state. The track parameters for the sites are summarized in Table 1. Data decompression of the selected, calibrated scenes, obtained from the EROS Data Center, was carried out with a JPL-supplied software package. Image processing and analysis were performed with the Earth Resources Mapper commercial software package. Image processing and data manipulation were carried out on σ° values. Uncertainties on σ° arise from SIR-C calibration uncertainties which have been published [*Freeman et al.*, 1995]. In general, we assume ±1 dB uncertainty (~ ±30%) on σ°. Cross talk between polarization channels is below -30 dB (<0.001). Any amplitude imbalance between HV and VH (<0.2 dB) is removed during calibration, and HV=VH is fixed. Further details regarding the radar image processing are described as necessary in the following sections.

3. Kunlun Shan

3.1. Geography

SIR-C DT 1/58.10 crosses western Tibet. The Kunlun Shan mountain range stretching from 75°E to 95°E at 35°N forms the border between the Tibetan plateau and the Tarim basin in western China [*Zuhui*, 1990]. The Kunlun Shan west of 80°30'E has 1180 glaciers covering 4331 km^2 [*Li and Cheng*, 1980; *Shih et al.*, 1980]. Many of the valley glaciers in the region are 20-30 km long [*Li and Li*, 1991]. Figure 4 shows the main glacier area of the western Kunlun Shan. The location of the scene selected for study is plotted in Figure 4.

The glaciers on the south slope of the western Kunlun Shan were explored by recent joint Chinese-Japanese glaciologic expeditions [*Watanabe and Zheng*, 1987]. *Zheng* [1987] provides 1:200,000-scale topographic maps of the Zhongfeng Glacier and Chongce Glacier and ice cap drainage areas. More detailed 1:50,000-scale topographic maps of the Chongce ice cap were produced [*Chen et al.*, 1989] in aid of ice coring studies [*Nakawo et al.*, 1989]. The ice core analyses [*Han et al.*, 1989] and the ice formation studies [*Ageta et al.*, 1989; *Xie and Zhang*, 1989] provide some measure of ground truth for the radar measurements. The

Table 1. SIR-C Quad-Pol Datatake (DT) Selections and Scene Processing Parameters

	DT 1/58.10		DT 2/40.60	
Name	Hotien East, China		Cerro Aconcagua	
Track angle	40.69° (Ascending)		142.82° (Descending)	
Look direction	South (Right)		South (Right)	
Image center	35.438°N, 80.966°E		33.407°S, 69.737°W	
Time				
GMT	1994/102:23:36:19.7		1994/275:21:51:49.9	
Local	05:06:19.7, April 13, 1994		17:51:49.9, Oct. 2, 1994	
Scenes				
L-band (24.0 cm)	pr14912		pr43677	
C-band (5.66 cm)	pr14913		pr43678	
θ_i				
Near range	29.042°		32.848°	
Image center	31.161°		34.674°	
Far range	33.083°		36.271°	
Shuttle roll angle	25.959°		25.987°	
Near slant range, km	245.4561		262.9919	
	DT 1/58.10		DT 2/40.60	
Scales	range	azimuth	range	azimuth
Slant range scene, km	10.254	49.996	10.707	49.999
Slant range pixels	1539	9599	1607	10251
Slant range pixel size, m	6.662	5.208	6.662	4.878
Ground range scene, km	19.816	49.996	18.82	49.999
Ground range pixel size, m	12.876	5.208	11.711	4.878
Multilook multiplier	2	5	3	7
Multilook pixels	769	1919	535	1464
Multilook pixel size, m	25.75	26.04	35.13	34.14

Note: Local time reported for the Hotien East scene is not the Chinese time zone, but the Indian time zone, UTC + 5.5 hours, which is closer to the true local time in the western Kunlun Shan. Local time for the Andes scene is the Chilean time zone, which is UTC - 4 hours.

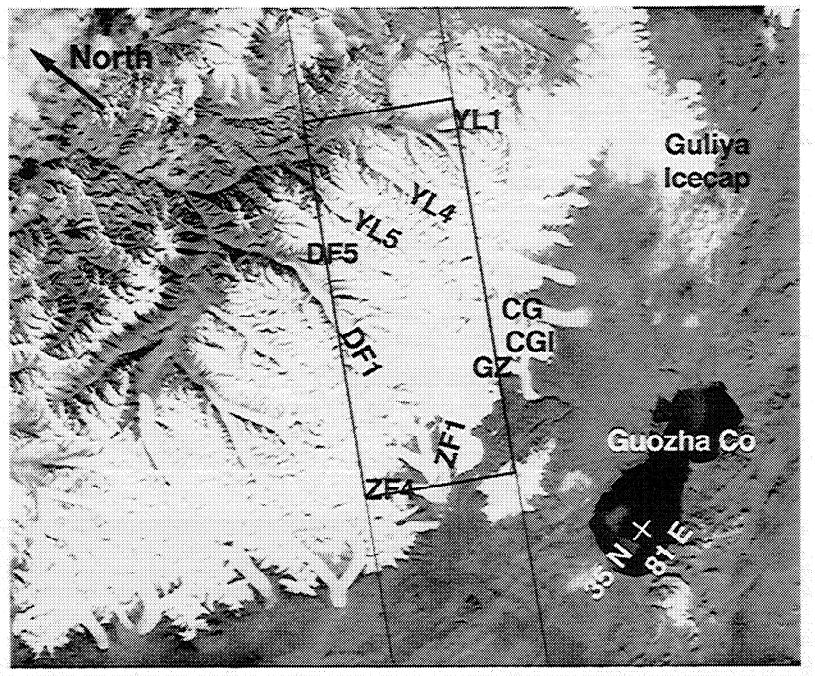

Figure 4. Excerpt from Space Shuttle handheld photograph (41G-0031-0042) of the western Kunlun Shan on October 6, 1984. SIR-C radar scene from track DT 1/58.10 of April 13, 1994, is outlined. Geographic locations in the radar scene are labeled and glacier names are abbreviated: ZF, Zhongfeng; GZ, Ghoza; CG, Chongce; CGI, Chongce Icecap; DF, Duofeng; YL, Yulong. Subglaciers are numbered. The image scale is approximately 105 km by 90 km.

north slope of the western Kunlun Shan has not been as intensively studied as the south. There, information is limited to 1:200,000-scale Russian topographic maps made from air photos dating from 1969 to 1973. These maps should be used with caution, as western Kunlun Shan glaciers advanced in the late 1970s [*Shih et al.,* 1980]. Additional Kunlun Shan glaciological information of a comparative nature is available from studies of the Guliya Icecap 30 km to the west of the Chongce Icecap [*Thompson*, 1996; *Thompson et al.*, 1995].

3.2. SAR Images

The image parameters for the L- and C-band scenes selected from DT 1/58.10 are listed in Table 1. A processed σ° image is shown in the lower panel of Figure 5. The band and polarization is CRL, where C refers to C-band and RL describes the circular-polarization state of the echo, i.e., transmitted right-polarized (R), received left (L). Topographic contours available from the Chinese maps have been drawn over the glaciers outlined in the separate cartoon. The most prominent characteristic of the image is the increasing cross section with altitude. The images for all the polarizations were examined. All the images display increasing σ° with altitude moving up the glaciers. While the different polarizations all increase with altitude, to interpret the radar scattering mechanisms and thereby infer ice properties, we are interested in the relative behavior of the different σ°. Labeled outlines on the σ° image are referred to below as sites for radar cross section statistics and angular scattering information.

3.3. Radar Cross Sections

A first assessment of the altitude-dependent behavior of the different polarizations was performed by examining scattering behavior moving up the glaciers. Statistics were calculated for wide regions (>1 km^2) at every 1000 m interval and are plotted for the Zhongfeng Glacier in Figure 6, and for Chongce Glacier in Figure 7. The average σ° values are tabulated in Table A1, Appendix A. Incidence angle variation was not considered for these plots but is investigated in section 3.5 for the sites labeled in Figure 5.

The σ°(CRL) values reach levels at 6200 m that are 2 or 3 times the average values observed by *Rignot et al.* [1993] over Greenland at similar incidence angle ($\theta_i \sim 30^\circ$). The highest σ°(LRL) values, on the other hand, are quite close to the level *Rignot et al.* [1993] report. These maximum σ° levels in circular-polarization occur in concert with maxima in the l inear-polarizations. The maximum linear cross-sections in both L- and C-bands are an order of magnitude larger than what *Forster et al.* [1996] found on the SPI in either fall (April) or summer (October) for their brightest scattering snow zone. The cross-polarized linear channel σ° are around 25% (-6 dB) of the copolarized σ°, which appears consistent with *Stiles and Ulaby's* [1980] observation for dry snow. It should be noted that DT 1/58.10 was taken early in the morning when the firn surface temperature would be nearer the diurnal minimum, and so we might expect that the near-surface conditions, dominating C-band in particular may have been particularly favorable to volume scattering.

3.4. Polarization Ratios

The behavior at C-band on both Zhongfeng (Figure 6) and Chongce (Figure 7) glaciers seems to indicate volume scattering, e.g. $\mu_l > 1/3$, above 6100 m, while the same ratio is somewhat subdued at L-band on both glaciers. The μ_c(C) behavior is similar at the higher elevations on both glaciers arriving at $\mu_c \sim 1$ above 6200 m. The μ_c (C and L) behavior on the lower reaches of the Chongce Glacier appears unique

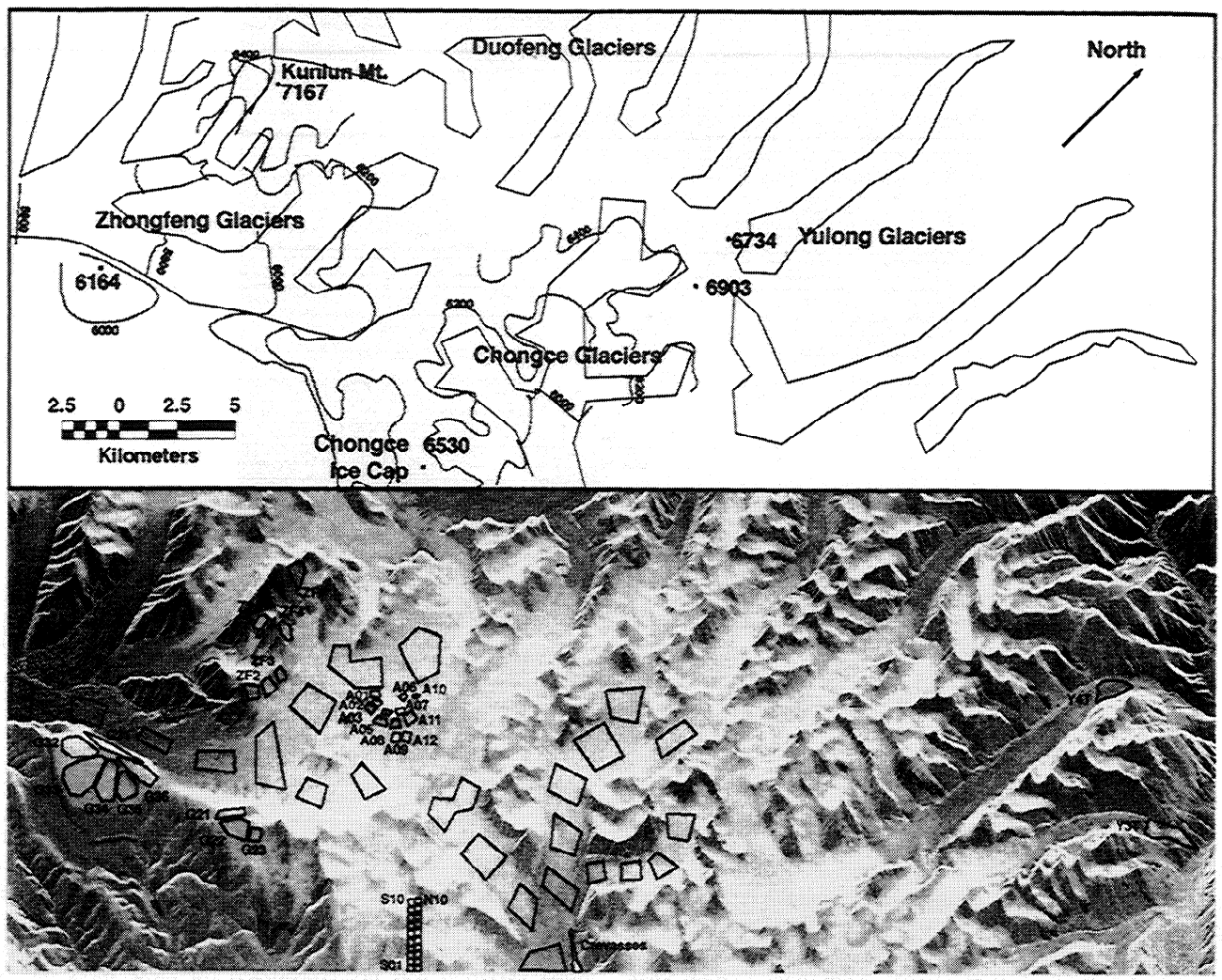

Figure 5. (lower panel) SIR-C Kunlun Shan σ°(CRL) image. Radar illumination is from the top, and SIR-C flight direction is to the right in the image. (upper panel) Cartoon with outlines of glaciers in the lower panel. Stippled lines in the upper panel are topographic contours from the Chinese maps for the western Kunlun south slope [*Zheng,* 1987]. Large polygons in the lower panel outline sites used for average profile analyses described in the text and plotted in Figures 6 (Zhongfeng) and 7 (Chongce). Small polygons with alphanumeric names are used for angular scattering behavior analysis as described in the text. Yulong Glacier toes are outlined at the right side of the lower panel, and the Chongce crevasse zone is outlined in the bottom middle.

from that exhibited by Zhongfeng, or indeed other glaciers in Figure 4. This is examined in more detail in section 3.7, below.

The regional behavior of the polarization ratios is plotted in Plate 1. Red color indicates $\mu_c>1$, white is $0.7<\mu_c<1$, green shows $0.25<\mu_c<0.7$, and blue indicates $\mu_c<0.25$. The ratios are calculated at each pixel based on median 5x5 filtered values of the σ°. The striking feature in all these polarization ratio figures is that the highest mountain slopes are red. In particular the highest feature in the scene, Kunlun Mountain, displays the most obvious μ_c inversion feature.

The ratio VV/HH is reported in the literature as a measure of surface versus volume scattering by snow [*Rott and Davis,* 1993; *Forster et al.*, 1996]. Low VV/HH (<1) is attributed to volume scattering from spherical snow grains while a higher ratio (>1.5) indicates surface scattering from wet snow [*Forster et al.*, 1996]. This is somewhat perplexing as in our case, VV/HH is >1.3 at all altitudes up the glaciers (Appendix A), which would suggest wet conditions everywhere. This seems unlikely for the local time and season of observation (Table 1). We note that our cross sections are also significantly greater than those observed in Patagonia by *Forster et al.* [1996] or in the Alps by *Rott and Davis* [1993]. *Rott and Davis* [1993] point out that incidence angle variations affect interpretation of VV/HH; still, we do not reproduce their observations for the snow cover of the Kunlun Shan.

3.5. Scattering Behavior

Angular scattering behavior can be examined if slopes are known at target sites. Forty-seven locations were chosen where slope reconstruction was feasible with the Chinese topographic maps [*Zheng*, 1987]. The locations and labels of

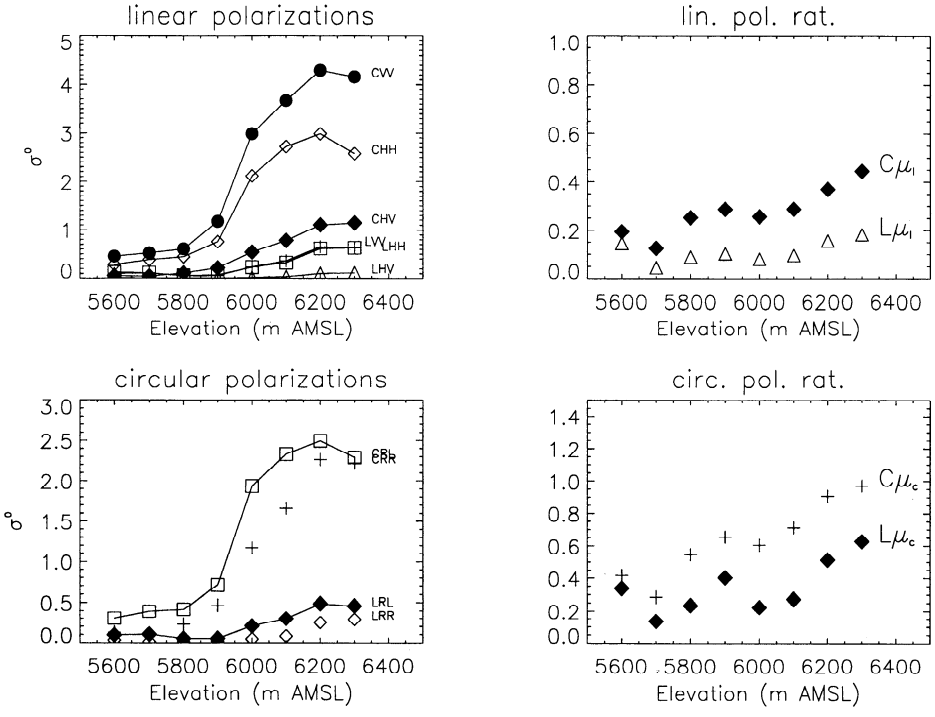

Figure 6. Plots of average radar scattering behavior at different altitudes on Zhongfeng Glacier 1. Left panels show cross-section behavior with altitude, right panels show polarization ratio behavior (ratios as defined in text and in Figure 3 caption). Top panels show linear-polarizations, bottom panels show circular. Statistics sampling regions are plotted by large polygons in Figure 5. The steep increase in cross section occurs at the snow line.

these sites are also shown in Figure 5. Twenty sites were placed in the radar range direction over the summit of the Chongce Icecap. Another 12 sites sample the radar data in the central portions of the Zhongfeng 1 Glacier's upper accumulation area. Six sites are located on the slopes around Kunlun Mountain west of Zhongfeng 1, and another nine are on the ice caps east of Zhongfeng 1 above 6000 m. All sites contain some pixels with C-band μ_c greater than unity. The

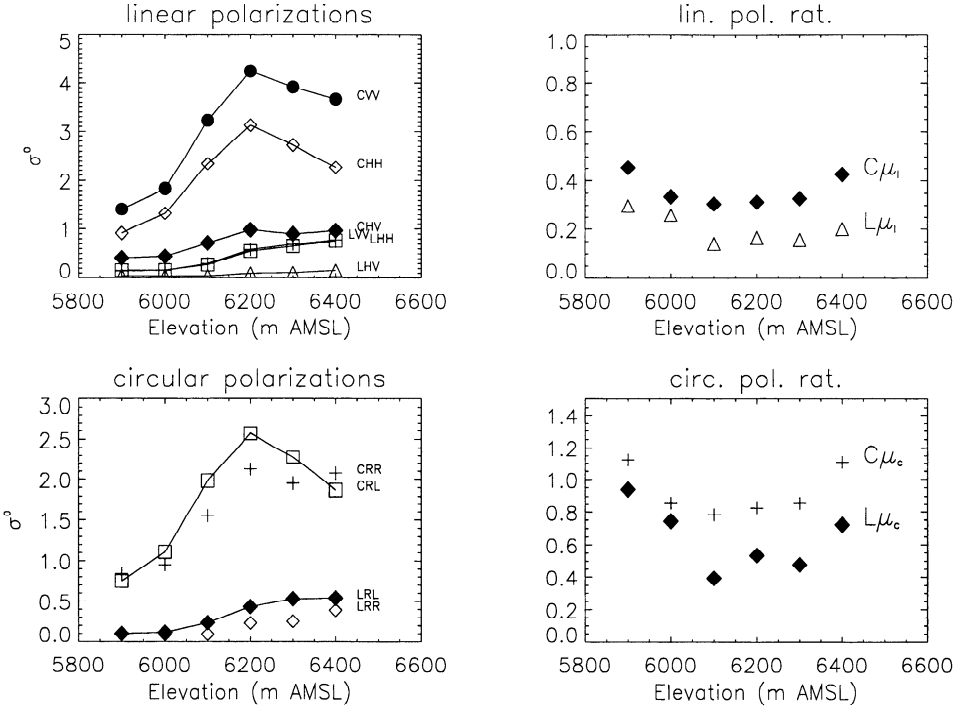

Figure 7. Plots of average radar scattering behavior at different altitudes on Chongce Glacier. Panels as in Figure 6. Statistics sampling regions are plotted by large polygons in Figure 5.

selected sites are spread over elevations from 6000 m up to 6500 m.

Averages were produced for all σ° values in the different polarization channels at each site and are tabulated in Appendix B. Radiometric slope corrections were applied to the average cross sections obtained from the images to account for the projected area of the target according to *van Zyl et al.* [1993]. The correction factors are in Appendix B. The angular scattering behaviors were so similar for all the groups of target sites that they could be plotted together. The results are shown in Figures 8 and 9. The overall similarity of scattering behavior, within the ±30% uncertainty, suggests that the behavior of $\mu_c>1$ sites is not very altitude-dependent above 6000 m.

The circular- (Figure 8) and linear-polarization (Figure 9) angular behaviors are highly correlated. For example, the distribution of σ°(LRL) points has a pattern very similar to that of the σ°(LHH) and σ°(LVV). This indicates that all the $\mu_c>1$ locales are uniformly bright in all polarization channels.

The polarization ratio and RL reflectivity behaviors that *Rignot* [1995] observed are plotted on the appropriate graphs in Figures 8 and 9 from the original data (E. Rignot, personal communication, 1997). It seems that while the σ°(CRL) values observed here are significantly higher than the Greenland results, the μ_c and μ_l behaviors at both C- and L-band show a strong resemblance to *Rignot et al.'s* [1993] observations. This similarity suggests a similar scattering mechanism. The linear cross sections here are significantly higher than *Rott and Mätzler's* [1987] pure dry-snow observations, corroborating the idea that icy inclusions are involved. We note also that in Figures 8 and 9 the scattering behavior does not match EGC: σ°(OC)>σ°(SC) at smaller incidence angles. The $\sigma^\circ_{OC}(\theta_i)$ is more specular than Lambertian, and the μ_c inversion disappears at small incidence angles even while σ° values increase.

3.6. Firn Properties

The strong suggestion that the scattering from the ice fields in the Kunlun Mountains SIR-C scenes is due to the presence of a percolation zone in the region is corroborated by field evidence. *Han et al.* [1989], *Xie and Zhang* [1989], and *Ageta et al.* [1989] all present firn stratigraphic sections for the Chongce Icecap. The sections all indicate icy inclusions, ice crusts, depth hoar or superimposed ice in the upper 2 m. The actual snow surface is otherwise unremarkable [*Nakawo et al.*, 1989]. The similarity of the radar behavior over the whole scene suggests that this firn structure is widespread in the Western Kunlun. Indeed, work on the Guliya Icecap [*Thompson*, 1996; *Thompson et al.*, 1995] has revealed similar structures (L. G. Thompson, personal communication, 1997).

The observed buried ice structures suggest a further consideration for the scattering behavior. If the structures are primarily ice layers as the snow sections suggest, then the decrease in μ_c at smaller incidence angles can be explained.

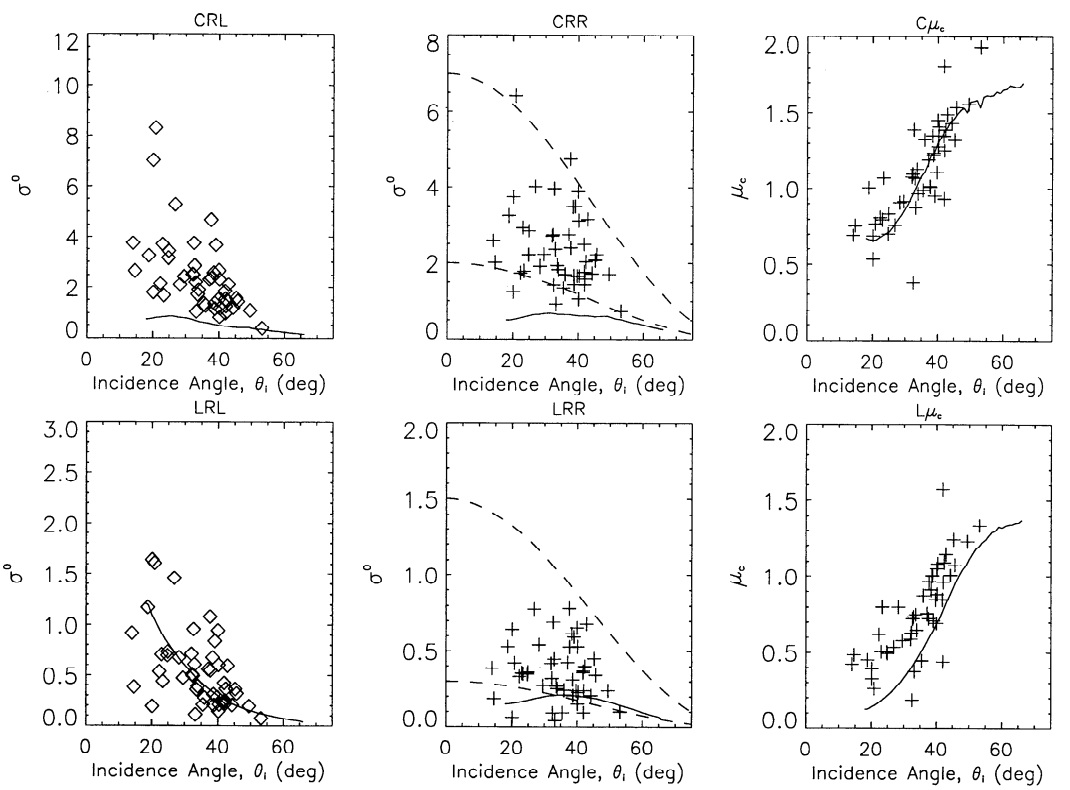

Figure 8. Circular-polarization angular scattering behavior for 47 sites in SIR-C Kunlun Mountain scenes. Site outlines are plotted in Figure 5 and described in text. The raw cross sections and slopes used to derive the values plotted here are listed in Appendix B. The solid lines in the σ°(RL) and μ_c plots are the average behavior observed in Greenland by *Rignot et al.* [1993]. The solid line in the σ°(RR) plot is derived from the other two lines. The dashed lines in the σ°(RR) plot represent A $\cos^2(\theta_i)$ scattering behavior for A values that bracket the data.

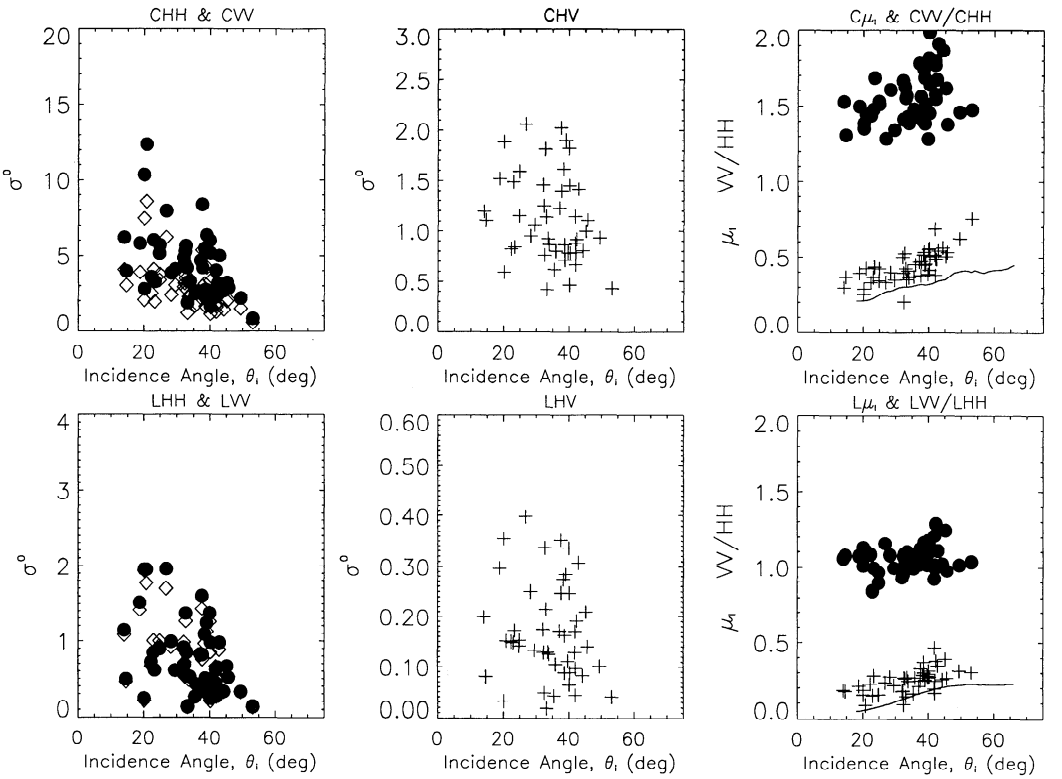

Figure 9. Linear-polarization angular scattering behavior for the same sites as Figure 7. Here the solid line in the μ_1 plots is the average μ_1 behavior that *Rignot et al.* [1993] observed. Symbols are HH, diamond; VV, filled circle; HV, cross, and the symbols for ratios correspond to the symbol of the numerator.

Rignot [1995] modeled the Greenland results with populations of ice cylinders. Ice layers can then be thought of as composed of these cylinders lying near horizontal. At small incidence angles the deviations of the cylinders from horizontal become less "apparent" to the incoming radar waves, and μ_c is less affected. In this fashion the decrease in μ_c is probing a fundamental quality of the evolution of the firn: ice inclusions in the firn produced from meltwater are aligned by gravity and by the sedimentary snow-layering of the firn.

The Tibetan plateau is subject to monsoonal precipitation. The Western Kunlun is an arid region, since the monsoonal flow is restricted by other intervening mountains. Here 70%-80% of the precipitation falls from May to September [*Zhang et al.*, 1989], with annual mean values around 30 cm on the top of the Chongce Icecap. The monsoon months of July and August also correspond to the warmest temperatures in the Western Kunlun, when snow wetting penetrates up to 25 cm at an elevation of 6100 m [*Takahashi et al.*, 1989]. Thus the April C-band radar measurements are likely probing to scatterers refrozen from the previous year's melting. The L-band σ°, on the other hand, may be integrating over several years' worth of scatterers. The difference in the ratio of L/C copolarized σ° to that obtained for Greenland may indicate differences in the scatterer populations. With field measurements of buried ice size and shape statistics, these differences might lead to a measure of the extent and amounts of the previous season's melting. This kind of quantification of radar scattering would make SAR polarimetry imaging more useful than imaging alone as a tool for glaciologists monitoring climatic effects on ice sheets [e.g., *Long and Drinkwater*, 1994].

3.7. Glaciologic Features

The The radar scattering results presented so far can be compared to the glaciological information for the Western Kunlun glaciers. The transitions from lower to higher σ° plotted in Figures 6 and 7 can be interpreted as bracketing the snow line on the two glaciers. The snow line on Zhongfeng Glacier would be around 5950 m, while on Chongce Glacier it appears to be around 6100 m. These transitions do in fact correspond to the published snow line levels. *Zhang and Jiao* [1987] report the snow line at 5965 m for Zhongfeng, and at 6120 m for Chongce. The difference in snow line levels for these two neighboring glaciers arises apparently from their different orientations relative to the westerly and southwesterly arrival of monsoonal precipitation [*Zhang and Jiao*, 1987]. That a transition is observed despite cold mid-April temperatures can be explained. Melting below the snow line would result in a fairly homogeneous ice mass. Homogeneous cold ice will backscatter less than the firn zone with icy inclusions present above the snow line. This technique of snow line detection from SAR single-polarization imagery was suggested by *Bindschadler and Vornberger* [1992] and is easily applied, provided topographic information exists for the SAR scene [*Albright et al.*, 1998].

Bindschadler and Vornberger [1992] also pointed out the use of SAR for detecting crevassed regions within the bare-ice (ablation) zone. The most likely candidate for a crevassed region in our images is the site on the northern edge of Chongce Glacier. The average properties of this radar-bright region are reported Table 2. The determination that this area is a crevasse zone is based on cartographic

Table 2. Chongce Glacier Crevasse Radar Properties

σ°(RL)	μ_c	σ°(HH)	μ_L	σ°(VV) / σ°(HH)
		C-band		
2.7±2.0 (0.2 to 15.3)	1.5±1.5	3.9±3.0 (0.3 to 18.1)	0.5±0.6	1.4±1.4
		L-band		
0.8±0.6 (0.1 to 5.9)	0.7±0.6	1.4±1.1 (0.1 to 9.8)	0.4±0.4	1.0±1.0

Note: Value ranges in parentheses. True incidence angle for the crevasse zone is $\theta_o \approx \theta_i - \alpha = 32.6^{\circ} - 2.3^{\circ} \approx 30.3^{\circ}$, where θ_i is incidence angle from the radar range distance of the Chongce crevasse site, and α is the slope of the Chongce glacier (toward radar).

information from *Zheng* [1987]. The reported strike direction of the crevasses is perpendicular to the glacier flow and thus to the SAR range direction. Since the location is below the snow line, and since the rest of the glaciers in the scene appear dark in the ablation zone, we can suppose that no significant snow layer covers the crevasses. Yet, both the circular and linear σ° are comparable to those observed on the Chongce Icecap for instance. Additionally, despite a low mean, L-band μ_c does exceed unity over much of this region, as can be seen in Plate 1b. In fact, the μ_c and μ_l values for both SIR-C wavelengths are on the high side of the scatter shown in Figures 8 and 9. These observations are consistent with *Rott and Davis'* [1993] observation of crevasse corner reflection behavior. However, we might expect to see other similarly bright regions associated with crevasses on Zhongfeng Glacier at 5800 m, which appears not to be the case. We suggest this is due to the preferred orientation of the crevasses on Chongce relative to the radar.

Further ambiguous radar behavior is demonstrated at the toes of glaciers. For example, we might expect that the tips of Yulong 3 and 4 both show similar radar behavior. They both appear oriented in a similar way to the radar, and their environments are also very similar. Yet, the toe of Yulong 3 has double the cross section of the toe of Yulong 4 and also has a more enhanced circular-polarization inversion. The average radar properties are listed in Table 3. The areas sampled at the glacier toes are outlined in Figure 5: Y3T and Y4T. The answer may well be that the structures at the toes are not identical. The glacier toes can be sites of intense melting, ice falls, and also perhaps of debris accumulation, all of which will vary the radar properties.

4. Central Andes

4.1. Geography

SIR-C DT 2/40.60 passes some 50 km south of the highest peak (6960 m) in the Americas, Cerro Aconcagua. South of Aconcagua, at the latitude of Santiago (33°20'S) on the Chilean-Argentinian border, is Cerro Tupungato (6570 m). Tupungato is the northernmost active volcano in Chile's southern volcanic zone [*Gerth*, 1955; *Zeil*, 1964]. Its smaller neighbor, Tupungatito (5278 m), has been active during this century. The poor level of information available on the Tupungato region as recently as the 1950s is reported by *Lliboutry*[1965b]. Chilean topographic information currently available has been relied on here [*Instituto Geographico Militar (IGM)*, 1985, 1994]. While published in 1994, it is based on a photogrammetric survey from 1955 and a terrain classification from 1965. The general slopes and features appear sound when compared with handheld shuttle photographs.

The modern snow line in the central Andes is around 4500 m at latitude 33°S [*Clapperton*, 1983]. *Lliboutry* [1956] has extensively studied the modern glaciers of the region. Some 30% of the terrain in the central Andes lies above this level [*Lliboutry*, 1965a, p.445], and some 50% of that is glaciated. The extent of glaciers in this decade can be assessed from the Shuttle handheld photograph shown in Figure 10. The track of DT 2/40.60 is plotted on Figure 10. The scene over Tupungatito that will be studied here is outlined. *Lliboutry* [1965b] estimated that 120 km^2 were covered by glaciers in the Tunuyan valley south of Tupungato.

Table 3. Glacier Toe Radar Properties

σ°(RL)	μ_c	σ°(HH)	μ_L	σ°(VV) / σ°(HH)
		Yulong 3, C-band		
1.14	1.05	1.44	0.4	1.42
		L-band		
0.36	0.95	0.52	0.32	1.09
		Yulong 4, C-band		
0.56	0.74	0.64	0.3	1.45
		L-band		
0.17	0.68	0.23	0.23	0.94

4.2. Central Andes Glacial Phenomena

The climate in the central Andes region is condusive to two distinct and somewhat peculiar glaciologic phenomena, rock glaciers and penetentes.

Rock glaciers, while not purely a glaciologic phenomenon, are often attributed to glacial processes [*Vitek and Giardino*,

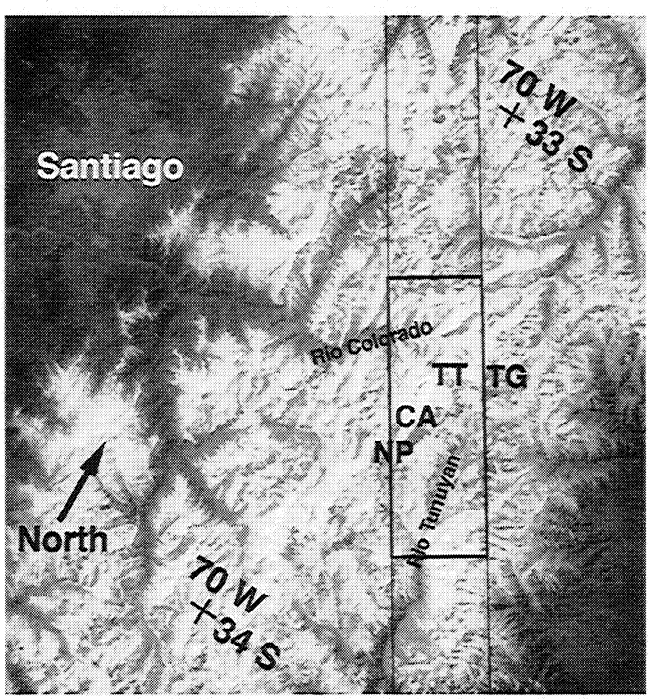

Figure 10. Excerpt from Space Shuttle astronaut handheld photograph from October 13, 1984 (STS41G-121-0045). The Tupungato radar scene from DT 2/40.60 on October 2, 1994, is outlined. Geographic features are labeled as follows: TG, Tupungato volcano; TT, Tupungatito volcano; CA, Cerro Alto; and NP, Nevado de los Piuquenes. The scale of the image is approximately 125 km by 130 km.

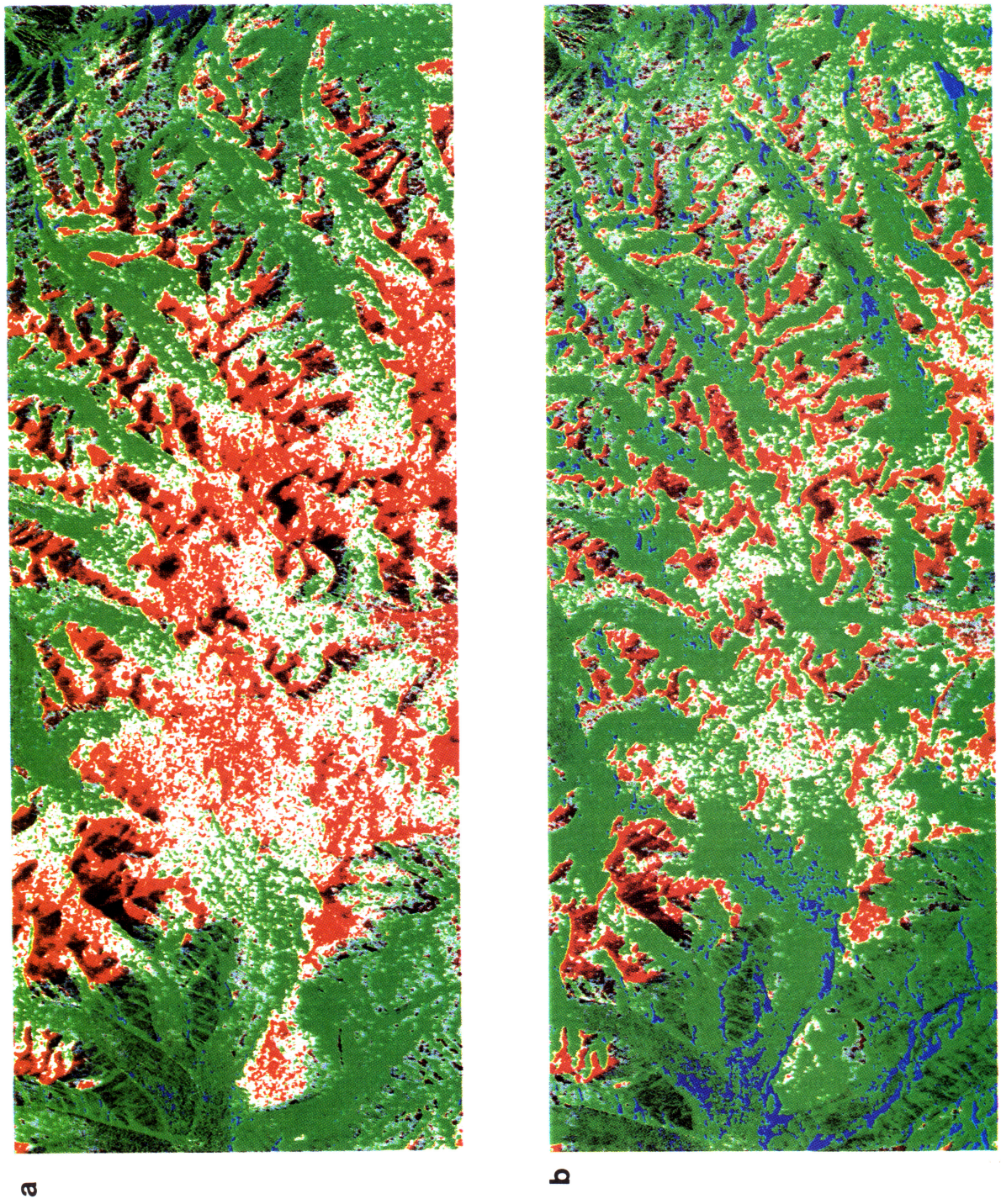

Plate 1. (a) Regional C-band circular-polarization ratio behavior in SIR-C Kunlun Mountain scene. Color assignments are red, $\mu_c > 1.0$; white, $0.7 < \mu_c < 1.0$; green $0.25 < \mu_c < 0.7$; and blue, $\mu_c < 0.25$. (b) Regional L-band circular-polarization ratio behavior in SIR-C Kunlun Mountain scene. Color assignment as in (a).

1987]. In the central Andes, rock glaciers are a common glacial phenomenon. The rock glacier morphology can be either as a debris-covered glacier or a fluid rock mass. In the central Andes, debris-covered glaciers exist, where the "debris responds as an active layer over the glacier ice which behaves as permafrost" [*Corte*, 1987]. The permafrost-like behavior is related to the altitude limits of permanent and seasonal freezing. In general, the depth of thawing at high elevations is around 20 cm at 4500 m, and at 60 cm or more at 4000 m. For radar remote sensing we might expect to identify rock glaciers as features in the landscape that resemble glaciers morphologically, yet do not display the radar behavior of either cold firn, ice, or wet ice surfaces. That is to say that the surfaces scatter diffusely with no signature of volume scattering expected. Yet, the surfaces should not be so smooth or absorbing as to be dark. Some measure of roughness might exhibit Bragg-like scattering behavior.

Penetentes are snow morphologies formed in a radiation-dominated environment. They can be quite unusual and spectacular in well-developed form appearing like a forest of wide snow blades standing on edge, aligned east to west [*Lliboutry*, 1965a]. They are understood to form in a radiation-dominated microenvironment on a snow or ice surface. An important point about penetentes that *Lliboutry* [1954] asserts is that the snow blades remain cold with frozen surfaces, while the snow or ground between the blades is wet or even slushy. This fact is confirmation of the thermal microenvironment that drives penetente formation. The radar signature of penetentes seems difficult to predict. Perhaps snow penetentes with refrozen troughs (at night?) or percolation features, might scatter in a similar manner to the percolation facies. Certainly, the existence of buried ice penetentes below a cold snow layer could cause significant volume scattering at the penetente-ice-blade/snow interfaces. In some sense these might behave like "vertical layers" of ice within the snowpack in contrast to the percolation facies' horizontal features. In the central Andes, *Lliboutry* [1954] lists penitentes of 2 cm forming at the beginning of June at 2650 m, of 8 cm forming at the beginning of September at 2900 m, and of 12 cm forming at 2700 m in mid-October. We might therefore expect penetentes to play a role in our October observations. Anecdotal mountaineering information (W. Pritti, personal communication, 1997) suggests that penetentes did not form in 1994 to any degree. Penetentes remain an interesting structure for future radar observations.

4.3. Radar Imaging

The image parameters for the DT 2/40.60 L- and C-band radar scenes over Tupungatito are listed in Table 1. We note that the image was acquired in the late afternoon, local time, when some amount of cooling of a snow surface would have occurred. Furthermore, handheld shuttle photographs of the central Andes taken (STS068-163-038), while not showing the Tupungatito region directly because of clouds, do show that the valleys were snow-covered down to 3500 m. An image of σ°(CRL) is shown in Figure 11. Prominent geographic features are labeled. Tupungato volcano itself is just off the top of the image.

What is not immediately apparent in Figure 11 is that the Tupugatito scene data were somewhat noisy. Some pixels appear to have been corrupted. They would appear with cross sections of up to 10^{30}! The affected pixels were different in the different polarization and frequency channels. The distribution of affected pixels over the scene was apparently random. Thus we applied a low-pass step-filter, keeping only pixels with $\sigma^\circ<1000$. The nulled pixels do not affect pixel statistics but will affect spatial filtering. Some remaining noisy pixels may be affecting some of the average cross sections.

The interpretation of the radar image is simplified with the use of a Shuttle handheld photograph taken during SRL-1. The April view of the Tupungatito region scene is shown in Plate 2a. The Tupungatito ice field is in the middle of the image, slightly left of center. The Nevado de los Piuquenes ice field is toward the bottom of Plate 2a, slighty right of center.

A comparison of the radar image in Figure 11 with Figure 4 of the Western Kunlun shows that there is no gradation in glacier properties with altitude: there are no glaciers long enough. The debris-free glaciers Tupungatito 1 and 2 and the debris-free glacier from Tupungato into the Rio Tunuyan valley are only moderately radar-bright in Figure 11, and show no indication of snow line or elevation related radar properties. The elevation of the terrain is insufficient, given the steepness of the slopes, for long glaciers. While the peaks are above 5000 m, the valley floors only 5 km away in the Rio Colorado valley for example are below 3500 m. This is far below the reported snow line, and it is not surprising that we can not observe a variation of glacier zones. An examination of Plate 2 and comparison with the topographic contours on Figure 11 confirm a lower limit of permanent ice at around 4000 m, and the snow line must lie somewhere above this.

4.4. Scattering Behavior

Circular-polarization ratio maps for the DT 2/40.60 scene are shown in Plates 2b and 2c. The color coding in the μ_c plots is the same as Plate 1. The ratios are calculated at each pixel as they were for the Western Kunlun scene. The scattered square white spots are due to the nulled pixels' effect on the 5x5 filter.

Both C-band polarization ratios (Plate 2b) are enhanced ($\mu_c>1$, $\mu_l\geq 1/3$) predominantly at those locations that had permanent ice at the end of the previous summer (Plate 2a). However, as we have mentioned, during the SRL-2 mission when DT 2/40.60 was acquired on October 2, all regions above about 3500 m were still snow-covered. Clouds in the Tupungatito region on October 2 would suggest that the high-altitude temperatures were near or below freezing when the image was obtained. The suggestion would be that the scattering is again due to icy scatterers within the cold frozen firn. Regions with $\mu_c>1$ in the polarization ratio maps (Plates 2b and 2c) are highly correlated with regions with $\mu_l>1/3$ (not shown), suggesting that volume scattering is occurring. This is not surprising given the radar transparency of cold firn and the scattering possibilities offered by icy inclusions.

Other features appear from a comparison of the L-band polarization ratio maps to the C-band ratio maps. On the north flank of the lower slope of Tupungatito there is an area (sites TV1-4) where $\mu_c(L)>\mu_c(C)$ and $\mu_l(L)>\mu_l(C)$. In the visible photograph (Plate 2a) the location also appears unremarkable (grey, not white). The polarization behavior is suggesting that some portion of the L-band echo is due to

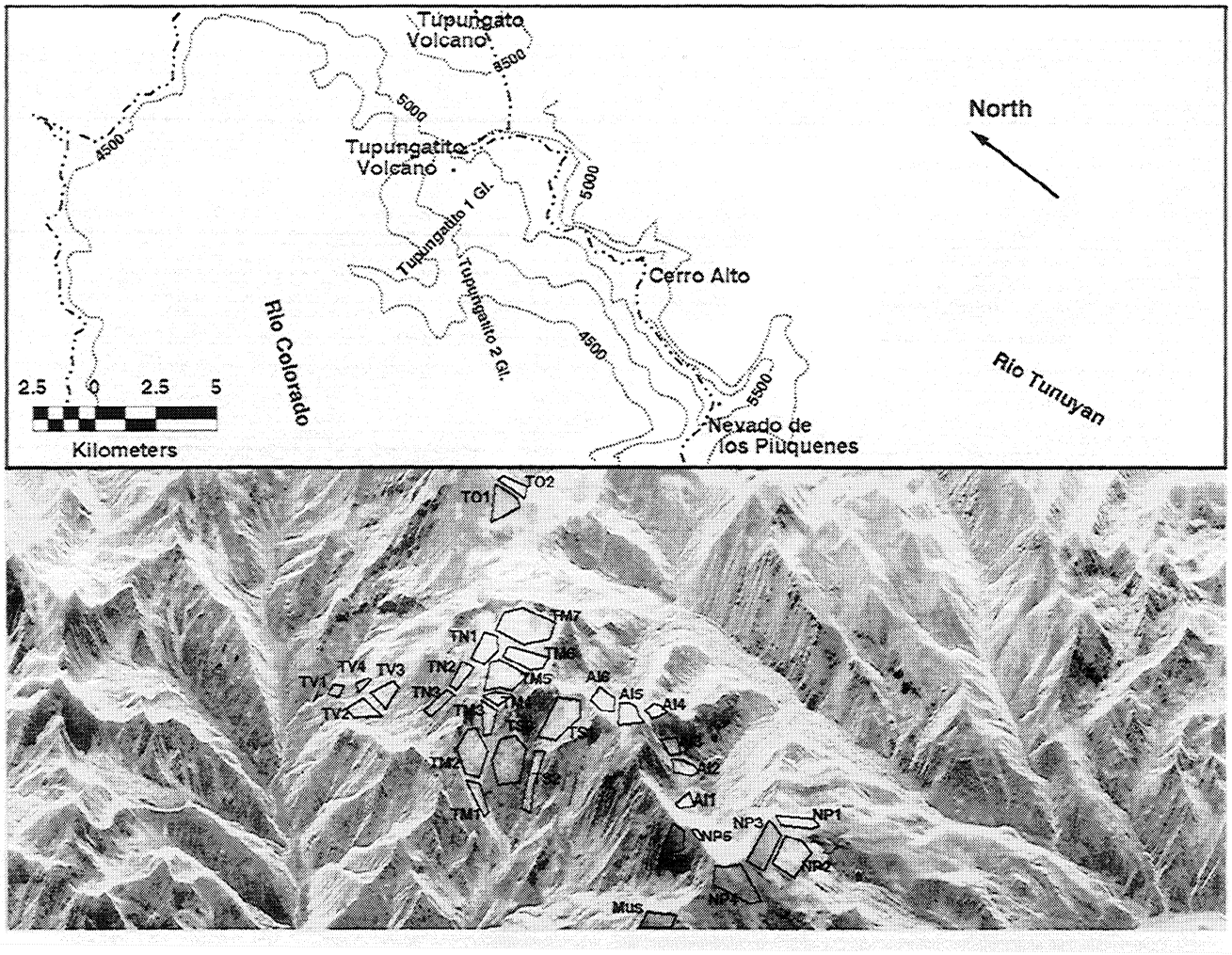

Figure 11. (lower panel) Radar σ°(RL) image of Tupungatito scene. Radar illumination is from the top, and SIR-C flight direction is to the right in the image. (upper panel) Labeled cartoon of topography and geography of lower panel. The drainage divide, which is also the international border in this region, is shown with a dash-double-dot line. The rio Colorado valley flowing toward the viewer is in Chile. Stippled topographic contours above 4500 m have been drawn from Chilean 1:50,000 section topographic maps "E" 61, and "E" 69 [*IGM*, 1985, 1994]. Polygons with alphanumberic labels in the lower panel outline sites used for angular scattering behavior analysis as described in the text.

volume scattering while C-band is being scattered to a greater degree at the surface. A thin layer of rock on the ice would affect the L-band less than the C-band and allow the L-band to scatter from the deeper icy layers. If this were borne out, it suggests an application of multiple-polarization radar monitoring of debris-covered glaciers.

The angular scattering behavior of the permanent ice regions in Plate 2a can be addressed as it was for the Kunlun Shan by sampling sites within the scene with different incidence angles. The slopes in this central Andes scene are somewhat steeper than those in the Western Kunlun. Thus there are more overlain (folded-over) features here. Note for example the mountain on the left edge of Figure 11 that lies on the border. Also, several dark regions on backslopes may well be shadowed (e.g., site NP6). Determining a scattering law requires careful assessment of the topography.

Sampling sites were picked in the image within regions of $\mu_c>1$. The locations were constrained to areas with coverage on Chilean topographic map sheets [*IGM*, 1985, 1994]. The sites picked are plotted on Figure 11. Of all the sites selected, only NP6 was clearly shadowed. Average scattering properties for all the sites shown in Figure 11 (except NP6) are plotted in Figure 12 for circular-polarization behavior, and in Figure 13 for linear-polarization behavior.

The scattering behavior of the four sites TV1-4 (shown by solid symbols in Figures 12 and 13) does appear to support the idea of L-band volume scattering. The C-band values are more reminiscent of scattering from the nearby rock surfaces (Plate 2a), while the L-band values are more like that for the other icy sites examined in the plots. Given that debris-covered glaciers do occur in the central Andes environment, the observations at the base of Tupungatito suggest that some component of the L-band σ° is from subsurface volume scattering by ice.

In Figure 12 we again observe that the μ_c behavior seems to track what *Rignot et al.* [1993] observed in Greenland. The match is only slightly poorer here in the central Andes than it was in the Western Kunlun. Of note, the low

a

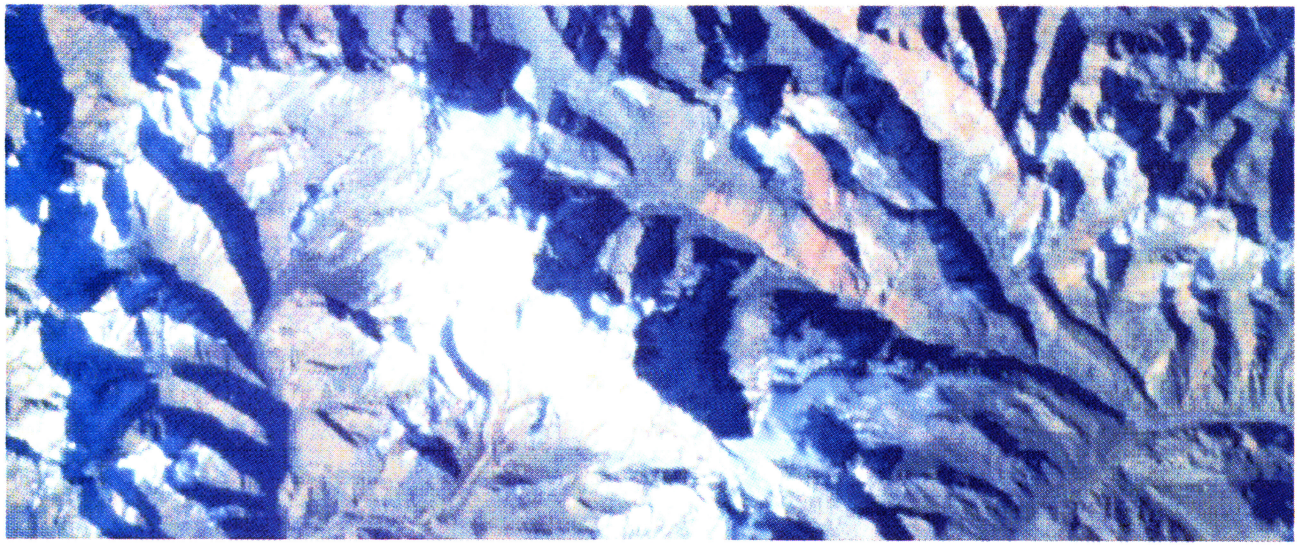

b

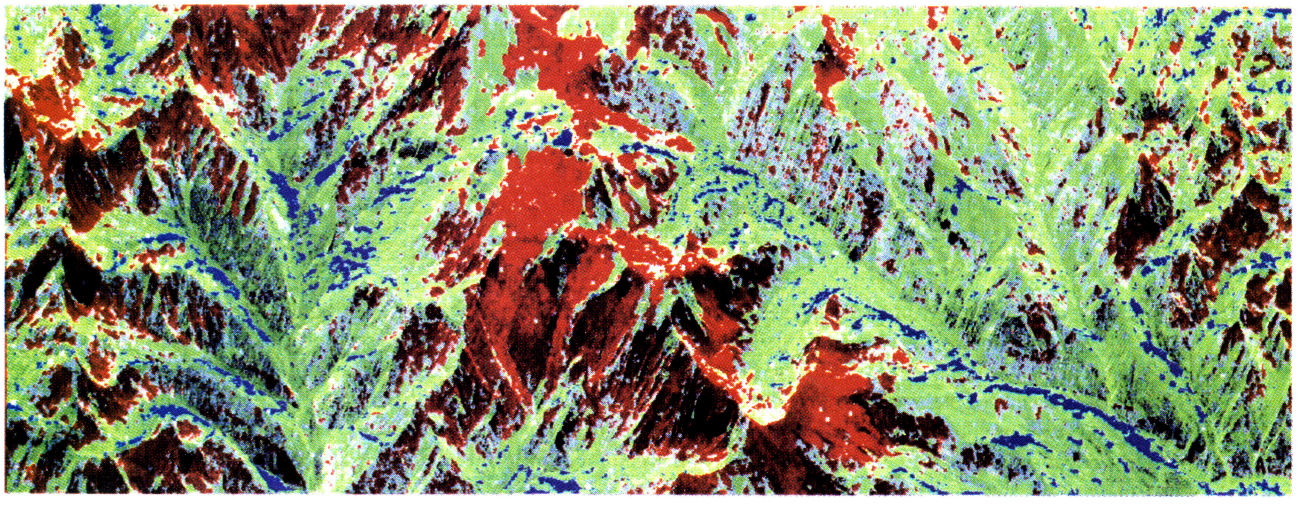

c

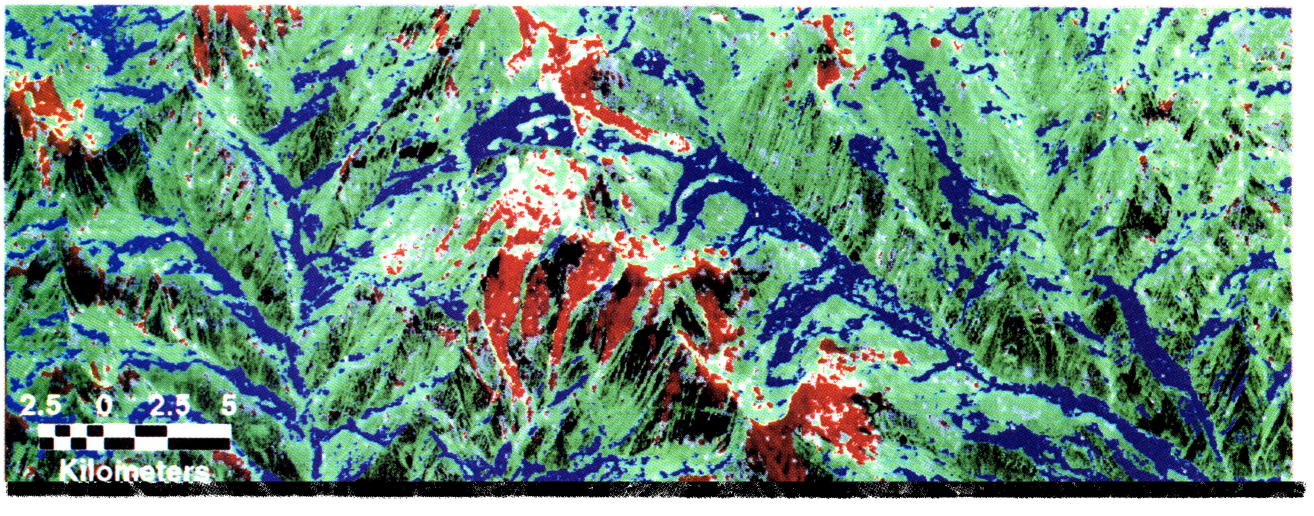

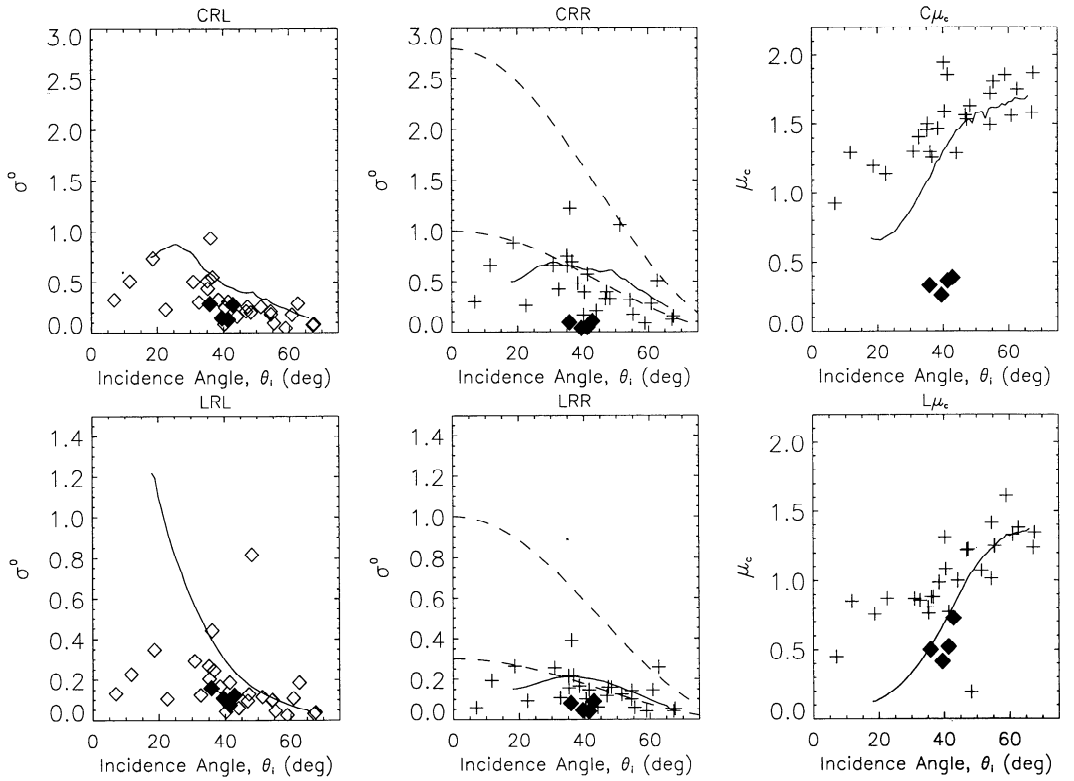

Figure 12. Circular-polarization angular scattering behavior for 31 sites in SIR-C Tupungatito volcano scenes. The raw cross sections and slopes used to derive the values plotted here are listed in Appendix B. The solid line in the σ°(RL) and μ_c plots is again the *Rignot et al.* [1993] Greenland behavior. The solid line in the σ°(RR) plot is deduced from the other two lines. The solid symbols correspond to the TV1-4 sites on the lower western flank of Tupungatito where $\mu_c(L)>\mu_c(C)$, suggesting L-band penetration to an enhanced volume-scattering region. The dashed lines in the σ°(RR) plot represent A $\cos^2(\theta_i)$ scattering behavior for A values that bracket the data.

incidence angle behavior appears to maintain the circular-polarization inversion below 20°. Also, the σ°(LRL) trends here, unlike the Kunlun (Figure 8) do not resemble what was measured in Greenland at $\theta_i<30°$.

5. Discussion and Conclusions

5.1. Greenland-Type Percolation Zone Scattering

We have examined the circular-polarization radar backscatter behavior of glaciers and ice fields at two high-elevation, midlatitude terrestrial sites, one in Tibet's Western Kunlun Shan, the other in the central Andes. Significant portions of the two sites exhibit high backscatter cross sections, σ°, coupled with circular-polarization ratio inversion, $\mu_c>1$, at both C- and L-band wavelengths (5.7 cm and 23.5 cm, respectively). The angular scattering behaviors of observed sites with $\mu_c\gtrsim1$ generally resembles that observed by *Rignot et al.* [1993] over Greenland. In situ information from the Western Kunlun in particular confirms buried ice structures in the regions exhibiting the unique radar behavior. This suggests that the Greenland ice scattering behavior is indeed widespread on Earth and would be observed for any glacier or ice field percolation zone under cold conditions when liquid water is absent.

Our observations do differ in some details from the earlier Greenland observations. (1) The σ°(CRL) and σ°(CRR) values in the Western Kunlun exceed those of Greenland. We suggest that this is not due to a difference of scattering

Plate 2. (opposite) (a) Excerpt from handheld Shuttle astronaut photograph STS059-L15-048 from the April SRL-1 mission, in southern hemisphere summer. The view toward the northeast from an orbit that is parallel to the October SRL-2 orbit when Tupungatito scenes were taken, views the scene with a perspective that mimics somewhat the ground range deformation of the southwest illuminating radar images. (b) Tupungatito region SIR-C C-band circular-polarization ratios. Red color indicates $\mu_c>1$, white $0.7<\mu_c<1.0$, green $0.25<\mu_c<0.7$, and blue $\mu_c<0.25$. The regions with permanent ice at the end of summer in (a) are those that primarily display $\mu_c>1$ in the SRL-2 spring scenes here. (c) Tupungatito region L-band circular-polarization ratios. Color assignments as in (b). Note that the upper reaches of the Tupungatito ice field on top of Tupungatito volcano display $\mu_c<0.7$ at L-band, while much of the rest of the permanent ice regions have $\mu_c>1$ where C-band μ_c is also greater than unity.

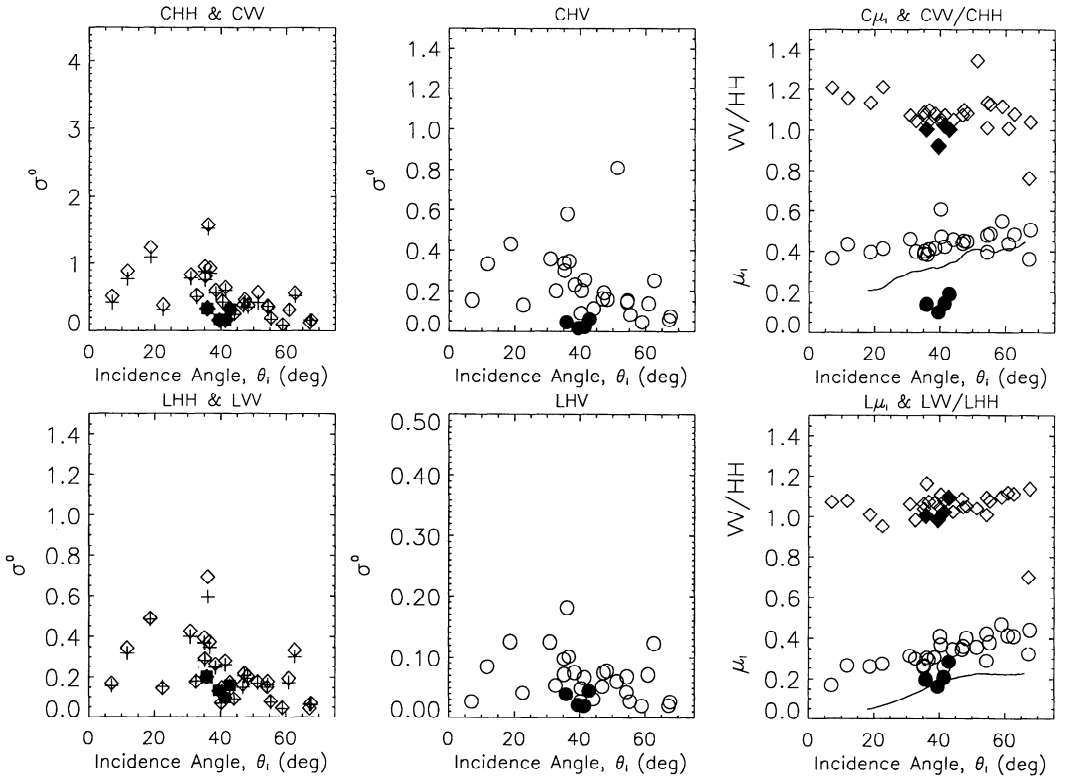

Figure 13. Linear-polarization angular scattering behavior for the same sites as Figure 12. Here the solid line in the μ_1 plots is the average μ_1 behavior that *Rignot et al.* [1993] observed. Symbols are: HH, cross; VV, diamond; HV, circle, and the symbols for ratios correspond to the symbol of the numerator. The solid symbols represent the Tupungatito lower western flank sites TV1-4 as in Figure 12.

mechanism but due to differences in the population of scatterers (icy inclusions). We base this suggestion primarily on the in situ information of the ice profile. (2) The μ_c(L) and μ_c(C) in the central Andes remain more elevated at smaller incidence angles than do the Greenland results. The corresponding σ° values are not otherwise exceptional and are, in fact, in line with the Greenland results. The likely reason for this is that our implicit assumption for our angular scattering study, that the scattering mechanism is independent of slope, is wrong. The anomalous points all correspond to steep slope locations where the snow hydrology may be quite variable and produce, for example, a vastly different population of embedded icy scatterers.

5.2. Planetary Analog Scattering Behaviors

In the same way as *Rignot* [1995], we must conclude that the percolation zone scattering behavior does not offer a

Table A1. Chongce and Zhongfeng Glacier Altitude Profile Average Radar Cross Sections

Altitude, m	σ° (CHH)	σ° (CHV)	σ° (CVV)	σ° (CRL)	σ° (CRR)	σ° (LHH)	σ° (LHV)	σ° (LVV)	σ° (LRL)	σ° (LRR)	N
					Chongce Glacier						
5900	0.914	0.414	1.415	0.749	0.841	0.148	0.044	0.156	0.101	0.095	2163
6000	1.33	0.446	1.84	1.111	0.952	0.159	0.041	0.164	0.117	0.087	3762
6100	2.349	0.718	3.228	1.984	1.554	0.298	0.042	0.277	0.236	0.093	5388
6200	3.128	0.981	4.243	2.573	2.126	0.586	0.097	0.552	0.433	0.232	6243
6300	2.726	0.895	3.914	2.279	1.954	0.693	0.109	0.654	0.529	0.253	4022
6400	2.267	0.963	3.665	1.873	2.073	0.776	0.156	0.763	0.538	0.389	5819
					Zhongfeng Glacier						
5600	0.283	0.055	0.455	0.302	0.126	0.096	0.014	0.128	0.095	0.032	1982
5700	0.383	0.048	0.523	0.392	0.112	0.11	0.005	0.115	0.104	0.014	3260
5800	0.444	0.112	0.608	0.416	0.227	0.056	0.005	0.06	0.051	0.012	1077
5900	0.757	0.217	1.177	0.712	0.466	0.058	0.006	0.074	0.052	0.021	1908
6000	2.114	0.542	2.988	1.935	1.17	0.236	0.019	0.23	0.206	0.046	3460
6100	2.721	0.781	3.671	2.331	1.66	0.361	0.035	0.323	0.297	0.081	4329
6200	2.986	1.104	4.294	2.494	2.261	0.651	0.102	0.615	0.486	0.249	5218
6300	2.576	1.144	4.16	2.289	2.22	0.631	0.115	0.631	0.458	0.287	3812

Table B1. Radar Cross Sections for Outlined Sites in Western Kunlun SIR-C Scenes

Site	N	Altitude, m	σ° (CHH)	σ° (CHV)	σ° (CVV)	σ° (CRL)	σ° (CRR)	σ° (LHH)	σ° (LHV)	σ° (LVV)	σ° (LRL)	σ° (LRR)	ϕ_s	α	θ_i
N01	100	6450	2.195	1.222	4.359	1.953	2.636	0.715	0.208	0.825	0.506	0.446	135.5	7.3	32.9
N02	100	6480	2.096	1.134	4.003	1.701	2.534	0.708	0.246	0.784	0.476	0.545	150.5	10.5	32.9
N03	100	6505	2.790	1.538	5.069	2.256	3.275	1.060	0.283	1.157	0.796	0.552	141.0	7.3	32.8
N04	100	6530	3.469	1.815	5.637	2.853	3.963	1.262	0.336	1.368	0.956	0.692	40.7	0.0	32.7
N05	100	6480	6.898	2.705	10.319	5.773	5.803	2.511	0.528	2.693	2.089	0.940	-26.5	16.1	32.7
N06	100	6410	11.991	3.541	18.305	11.094	7.684	3.196	0.590	3.378	2.721	1.146	-26.0	23.7	32.6
N07	100	6270	2.294	0.936	3.280	1.739	1.960	0.487	0.131	0.535	0.364	0.273	40.5	8.8	32.6
N08	100	6270	1.214	0.833	2.148	0.925	1.673	0.346	0.161	0.418	0.222	0.349	53.5	21.1	32.5
N09	100	6335	5.067	1.917	7.914	4.433	4.497	1.352	0.333	1.514	1.023	0.741	54.0	13.5	32.4
N10	100	6305	3.573	1.179	5.131	3.077	2.496	0.956	0.214	1.034	0.769	0.476	-30.7	10.9	32.4
S01	90	6425	2.771	1.425	4.826	2.284	3.082	0.852	0.242	0.962	0.597	0.544	175.5	7.3	32.9
S02	90	6455	3.904	1.774	5.908	3.422	3.260	1.050	0.265	1.154	0.783	0.555	-155.0	14.4	32.9
S03	90	6470	2.931	1.381	4.129	2.346	2.366	0.745	0.244	0.805	0.541	0.521	-146.3	15.8	32.8
S04	90	6460	1.611	0.857	2.717	1.361	1.661	0.434	0.161	0.499	0.308	0.309	-146.0	17.8	32.8
S05	90	6440	3.127	1.244	5.024	2.762	2.505	1.201	0.327	1.295	0.884	0.708	-110.5	15.4	32.7
S06	90	6415	7.767	2.580	9.965	6.599	5.027	2.127	0.498	2.453	1.824	0.975	-98.5	10.4	32.6
S07	90	6345	2.646	1.145	4.456	2.284	2.445	0.842	0.234	0.836	0.597	0.479	-59.0	9.4	32.6
S08	81	6330	1.791	0.692	2.297	1.323	1.464	0.352	0.098	0.357	0.249	0.211	69.0	12.4	32.5
S09	90	6380	3.744	0.760	5.274	3.747	1.425	0.522	0.048	0.559	0.495	0.092	40.7	0.0	32.5
S10	90	6330	3.452	0.991	4.663	3.009	2.073	0.355	0.054	0.400	0.322	0.105	-78.0	15.4	32.4
G21	506	6180	2.751	1.164	4.270	2.251	2.406	0.843	0.219	0.864	0.619	0.456	-138.5	10.2	31.7
G22	1038	6180	1.522	0.738	2.547	1.180	1.639	0.408	0.154	0.524	0.294	0.321	174.5	13.4	31.8
G23	356	6120	1.483	0.746	2.396	1.167	1.543	0.399	0.156	0.496	0.271	0.336	120.5	13.5	31.9
G31	722	6080	11.961	3.021	16.563	11.262	6.001	3.095	0.568	3.124	2.627	1.031	-20.0	13.9	31.2
G32	1400	6100	3.234	1.128	4.343	2.585	2.365	0.651	0.141	0.648	0.503	0.291	-115.0	4.7	31.2
G33	2731	6100	1.506	0.557	2.227	1.224	1.210	0.236	0.038	0.234	0.189	0.084	175.5	5.5	31.4
G34	1603	6060	1.377	0.522	2.172	1.205	1.122	0.206	0.034	0.209	0.167	0.073	113.3	10.9	31.5
G35	1078	6080	1.154	0.405	1.810	1.019	0.891	0.126	0.018	0.131	0.107	0.040	54.0	6.2	31.3
G36	1086	6100	2.255	0.823	3.127	1.804	1.742	0.488	0.119	0.500	0.371	0.240	60.0	6.2	31.4
ZF1	460	6120	0.894	0.370	1.299	0.656	0.838	0.163	0.051	0.192	0.114	0.120	113.0	9.8	30.7
ZF2	425	6120	1.566	0.705	2.293	1.135	1.502	0.345	0.092	0.371	0.244	0.213	86.0	7.0	30.7
ZF3	266	6180	1.294	0.580	1.791	0.946	1.167	0.240	0.072	0.279	0.167	0.167	124.0	8.2	30.6
ZF4	391	6400	1.525	0.948	2.227	1.120	1.744	0.328	0.103	0.333	0.199	0.244	50.7	35.8	30.2
Z2A	429	6500	1.571	0.833	2.164	1.086	1.669	0.398	0.105	0.389	0.240	0.258	178.5	19.8	30.2
ZF5	644	6700	0.596	0.449	0.879	0.402	0.777	0.138	0.042	0.143	0.078	0.104	51.0	40.8	29.7
A01	166	6280	3.053	1.528	5.087	2.646	2.848	1.028	0.182	0.957	0.745	0.438	37.0	12.2	30.7
A02	91	6300	4.992	2.105	7.539	4.539	3.792	1.324	0.202	1.184	0.970	0.478	2.0	12.2	30.8
A03	181	6320	1.094	0.614	2.041	0.920	1.318	0.247	0.063	0.252	0.156	0.157	171.0	16.1	30.9
A04	85	6340	4.140	1.414	6.327	3.866	2.717	1.148	0.173	1.109	0.852	0.429	-41.0	6.2	30.9
A05	228	6340	1.252	0.611	1.936	0.987	1.235	0.306	0.075	0.304	0.194	0.186	158.0	12.2	30.9
A06	78	6380	6.999	2.561	9.144	6.145	4.665	1.061	0.187	1.140	0.888	0.430	-71.0	19.1	30.7
A07	112	6380	5.387	1.963	7.945	4.878	3.889	1.326	0.195	1.116	0.931	0.470	-63.0	8.2	30.9
A08	181	6350	1.238	0.624	2.030	0.944	1.331	0.262	0.071	0.291	0.168	0.182	151.0	9.8	31.0
A09	169	6320	3.329	1.312	4.703	2.643	2.898	0.753	0.135	0.716	0.535	0.337	-135.0	12.2	31.1
A10	49	6360	12.866	5.450	18.552	12.473	9.624	2.649	0.227	2.928	2.412	0.631	-20.0	12.2	30.7
A11	253	6360	1.768	0.907	3.182	1.464	1.973	0.526	0.102	0.485	0.335	0.284	89.0	13.5	30.9
A12	177	6310	2.374	1.111	4.227	2.098	2.496	0.735	0.155	0.747	0.507	0.384	62.0	12.2	31.1

Alphanumeric site names are shown by polygon in Figure 5. N is the number of pixels inside the polygon. Altitude is determined from *Zheng* [1987]. Radar cross sections are labeled by three letters. The first letter is the wavelength band, C (5.6 cm) or L (23.5 cm). The second and third letters are for the transmitted and received polarizations, respectively: L, left-circular; R, right-circular; H, horizontal; V, vertical. The ϕ_s is the angle clockwise from the radar track direction to the polygon dip azimuth, α is the polygon dip measured positive down from horizontal, and θ_i is the incidence angle at the polygon if it were horizontal.

good analog for EGC. The backscatter σ° values are more peaked at small incidence angle (more specular) for all polarizations than the EGC scattering models allow. Our observations of high backscatter cross section echoes from crevasses, however, offer a possible avenue for future investigations. Likewise, the variable echoes from probable pure-ice glacier toes suggest another terrestrial locale to explore the ice morphological constraints on radar scattering.

5.3. Remote Sensing Applications

While various linear-polarization combinations are commonly used to identify different snow and ice surfaces with

SAR imaging [*Forster et al.*, 1996; *Albright et al.*,1998], the circular-polarization ratio, in particular, appears well-suited to identifying percolation zones. Monitoring of the seasonal and interannual variation of percoaltion zone spatial extent may provide remotely sensed input information for hydrologic monitoring.

Our modest evidence for penetration through a rock covering into glacier ice with L-band in the central Andes suggests a remote monitoring scheme for rock-covered glaciers using longer wavelength multi-polarization SAR. This would provide a means to account for these camouflaged glaciers' contents in hydrologic mass balance studies. Furthermore, it may contribute further to the study of EGC analogs, where silicates are mixed with the ices.

Appendix A: Western Kunlun Glacier Profiles

Average σ° values at various elevations on Chongce and Zhongfeng glaciers are tabulated in Table A1. The sample areas for these averages are the larger, unlabeled polygons shown in the lower panel of Figure 5. The polygons straddle elevation contour lines every 1000 m, as shown in the upper panel of Figure 5.

Appendix B: Incidence Angle Radiometric Correction and Angular Scattering Results

We wish to examine the angular scattering behavior of subregions within our chosen SIR-C radar images. In order to carry out image analysis on radar images, three types of corrections are typically applied to terrestrial radar data. The first is a correction for variations in pixel size due to topography, the second is a correction for Lambert's cosine law, and the third is a correction for the target specific scattering properties [e.g., *Albright et al.*, 1998; *Ulander*, 1996; *van Zyl et al.*, 1993]. These corrections are carried out to make comparisons and classifications of different parts of an image quantitatively meaningful.

In our case we are particularly interested in the target's specific scattering properties and so do not want to "correct" for them. Furthermore, since we are comparing to planetary radar work, where the Lambert cosine law is incorporated in

Table B2. Radar Cross Sections for Outlined Sites in Central Andes / Tupungatito SIR-C Scenes

site	N	Altitude, m	σ° (CHH)	σ° (CHV)	σ° (CVV)	σ° (CRL)	σ° (CRR)	σ° (LHH)	σ° (LHV)	σ° (LVV)	σ° (LRL)	σ° (LRR)	ϕ_s	α	θ_i
Al1	205	4470	0.566	0.226	0.592	0.340	0.478	0.203	0.061	0.200	0.140	0.120	124.0	11.3	34.7
Al2	396	4370	0.456	0.215	0.472	0.265	0.421	0.144	0.053	0.160	0.099	0.107	144.0	21.8	34.5
Al3	314	4950	0.126	0.064	0.131	0.068	0.127	0.050	0.022	0.057	0.032	0.043	176.0	43.9	34.3
Al4	260	5500	2.083	0.826	2.362	1.399	1.673	0.923	0.241	0.933	0.665	0.503	77.0	18.4	34.1
Al5	539	5600	3.445	1.261	4.163	2.652	2.447	1.278	0.217	1.375	1.063	0.478	41.5	30.6	34.1
Al6	522	4300	2.357	1.027	2.723	1.570	2.034	0.981	0.260	1.061	0.698	0.595	65.5	24.0	34.0
Mus	595	4900	0.102	0.037	0.078	0.050	0.079	0.040	0.013	0.028	0.021	0.026	-116.5	32.0	35.5
NP1	502	4800	0.953	0.439	1.021	0.619	0.806	0.489	0.154	0.521	0.359	0.312	116.5	14.0	34.8
NP2	1285	4700	0.417	0.796	0.560	0.252	1.038	0.168	0.060	0.175	0.114	0.122	156.0	32.0	35.1
NP3	1115	5400	0.151	0.092	0.159	0.085	0.165	0.066	0.027	0.069	0.042	0.055	150.0	16.7	35.0
NP4	1497	5250	0.060	0.033	0.067	0.034	0.063	0.030	0.014	0.033	0.018	0.029	-161.5	26.6	35.3
NP5	78	5750	1.175	0.486	1.423	0.846	0.965	0.560	0.153	0.533	0.388	0.338	94.0	32.0	34.9
TM1	425	4250	0.280	0.126	0.303	0.158	0.257	0.152	0.061	0.160	0.640	0.124	-164.0	15.9	34.7
TM2	1385	4700	0.223	0.107	0.253	0.128	0.220	0.114	0.048	0.125	0.070	0.099	-116.0	20.3	34.4
TM3	498	5100	0.328	0.159	0.354	0.183	0.320	0.190	0.078	0.212	0.118	0.163	-123.5	28.6	34.1
TM4	292	5270	0.510	0.216	0.547	0.262	0.486	0.220	0.057	0.238	0.160	0.124	-99.2	8.2	34.0
TM5	1203	5470	0.508	0.211	0.549	0.301	0.441	0.225	0.069	0.241	0.153	0.151	-65.0	8.5	33.8
TM6	807	5590	0.850	0.329	0.923	0.498	0.724	0.358	0.095	0.382	0.260	0.210	-53.0	4.4	33.7
TM7	2007	5600	0.727	0.291	0.779	0.423	0.634	0.271	0.070	0.282	0.198	0.151	-53.0	5.2	33.5
TN1	706	5470	0.799	0.327	0.876	0.518	0.652	0.327	0.096	0.352	0.232	0.205	-60.0	6.7	33.6
TN2	418	5280	0.333	0.151	0.366	0.203	0.311	0.163	0.059	0.171	0.102	0.125	-84.5	16.7	33.8
TN3	399	4850	0.218	0.100	0.229	0.141	0.182	0.078	0.027	0.080	0.053	0.053	-63.0	17.4	34.0
TO1	849	5750	0.257	0.102	0.260	0.146	0.218	0.104	0.030	0.105	0.068	0.069	-160.0	24.2	32.6
TO2	357	5750	2.500	0.958	2.588	1.540	2.003	0.980	0.299	1.141	0.727	0.643	125.0	31.0	32.4
TS1	1481	5250	0.298	0.131	0.320	0.171	0.267	0.121	0.042	0.132	0.077	0.094	-80.0	16.7	34.1
TS2	744	4250	0.212	0.093	0.214	0.120	0.187	0.116	0.048	0.130	0.073	0.097	-103.0	27.8	34.6
TS3	1704	4500	0.119	0.058	0.134	0.066	0.119	0.050	0.019	0.054	0.032	0.040	-122.0	21.0	34.4
TV1	169	3700	0.167	0.017	0.154	0.142	0.037	0.130	0.021	0.128	0.106	0.044	-45.5	16.7	33.9
TV2	545	4000	0.364	0.051	0.365	0.314	0.104	0.218	0.043	0.219	0.174	0.087	-31.3	16.7	34.0
TV3	507	4550	0.315	0.060	0.316	0.271	0.105	0.155	0.044	0.170	0.120	0.087	-47.3	21.8	34.0
TV4	125	4450	0.138	0.020	0.141	0.118	0.043	0.087	0.018	0.089	0.069	0.036	-57.0	15.3	33.9

Alphanumeric site names are shown by polygon in Figure 5. N is the number of pixels inside the polygon. Altitude is determined from *Zheng* [1987]. Radar cross sections are labeled by three letters. The first letter is the wavelength band, C (5.6 cm) or L (23.5 cm). The second and third letters are for the transmitted and received polarizations, respectively: L, left-circular; R, right-circular; H, horizontal; V, vertical. The ϕ_s is the angle clockwise from the radar track direction to the polygon dip azimuth, α is the polygon dip measured positive down from horizontal, and θ_i is the incidence angle at the polygon if it were horizontal.

the scattering law, we only need to correct for pixel size variations caused by topography. So, following *van Zyl et al.* [1993],

$$\sigma^\circ_{corr} = \sigma^\circ f_{corr} \quad \text{(A1)}$$

or more specifically,

$$\sigma^\circ_{corr} = \sigma^\circ \, (\sin(\theta_i - \theta_r) \cos \theta_a) \, / \, \sin \theta_i \quad \text{(A2)}$$

where σ° is the uncorrected radar cross section, f_{corr} is the correction factor, σ°_{corr} is the corrected radar cross section, θ_i is the incidence angle to a locally flat surface, θ_r is the tilt of the surface in the radar range direction, with $\theta_r>0$ for tilt toward the radar, and θ_a is the tilt of the surface along the radar track direction, with $\theta_a>0$ for tilts in the direction of radar motion. Then if we define the local slope of a target region in the radar image with ϕ_o the angle between the dip azimuth and the SIR-C ground track azimuth, positive clockwise, and with α the dip angle positive down from horizontal,

$$\theta_r = \arctan(-\tan \alpha \sin \phi_o) \quad \text{(A3)}$$

and

$$\theta_a = \arctan(-\tan \alpha \cos \phi_o) \quad \text{(A4)}$$

Replacing (A3) and (A4) in (A2), we get

$$f_{corr} = (\sin(\theta_i - \arctan(-\tan \alpha \sin \phi_o)) \cos (\arctan(-\tan \alpha \cos \phi_o))) \, / \, \sin \theta_i \quad \text{(A5)}$$

Additionally, if we let $\boldsymbol{n}$ be the unit normal vector to the target facet,

$$\boldsymbol{n} = (\sin \alpha \sin \phi_o, \ \sin \alpha \cos \phi_o, \ \cos \alpha) \quad \text{(A6)}$$

and if $\boldsymbol{R}$ is a unit vector from the radar to the facet, then from the cosine definition of the dot product we get θ_o, the true incidence angle at the facet,

$$\theta_o = \arccos(\cos \alpha \cos \theta_i - \sin \alpha \sin \phi_o \sin \theta_i) \quad \text{(A7)}$$

The data in Tables B1 and B2 are the raw cross section data and the topographic slope azimuth and dip needed to calculate f_{corr} and θ_o for Figures 8, 9, 12, and 13.

Acknowledgments. We gratefully thank Ellen O'Leary for her expeditious help in acquiring SIR-C data, as well as all the members of the SIR-C mission who made data mining on the World Wide Web possible. Tom Farr, Eric Rignot, Bruce Chapman, Lonnie Thompson, Miriam Jackson, Eric Fielding, Kay Campbell, Irma Black, and Willi Pritti all helped with useful discussions, data, or experience. This work was funded by NASA Planetary Geology grant NAGW-3011. California Institute of Technology contribution 5760.

References

Ageta, Y., W. Zhang, and M. Nakawo, Mass balance studies on Chongce Ice Cap in the West Kunlun Mountains, *Bull. Glacier Res.*, *7*, 37-45, 1989.

Albright, T. P., T. H. Painter, D. A. Roberts, J. Shi, J. Dozier, and E. Fielding, Classification of surface types using SIR-C/X-SAR, Mount Everest area, Tibet, *J. Geophys. Res.*, *103*, 25823-25838, 1998.

Benson, C.S., *Stratigraphic Studies in the Snow and Firn of the Greenland Ice Sheet, Rep. 10*, U. S. Army Snow Ice and Permafrost Res. Estab., 1962.

Benson, C.S., C.S. Lingle, and K. Ahlnaes, Glacier facies on Mt. Wrangell examined by SAR imagery (abstract), Fall Meet. Suppl., *EOS Trans. AGU*, *78*(46) F195, 1996.

Bindschadler, R., and P. Vornberger, Interpretation of SAR imagery of the Greenland Ice Sheet using coregistered TM imagery, *Remote Sens. Environ.*, *42*(3), 167-175, 1992.

Bindschadler, R., K.C. Jezek, and J. Crawford, SEASAT observations of Greenland, *Ann. Glaciol.*, *9*, 11-19, 1987.

Butler, B.J., 3.5-cm Radar investigation of Mars and Mercury: Planetological implications, Ph.D. thesis, Calif. Inst. of Technol., Pasadena, Calif., 1994.

Butler, B.J., D.O. Muhleman, and M.A. Slade, Mercury full-disk radar images and the detection and stability of ice at the North Pole, *J. Geophys. Res.*, *98*, 15003-15023, 1993.

Campbell, D. B., J. F. Chandler, G. H. Pettengill, and I. I. Shapiro, Galilean satellites of Jupiter: 12.6-centimeter radar observations, *Science*, *196*, 650-653, 1977.

Chen, J., Y. Wang, L. Liu, and P. Gu, Surveying and mapping on the Chongce Ice Cap in the West Kunlun mountains, *Bull. Glacier Res.*, *7*, 1-7, 1989.

Clapperton, C.M., The glaciation of the Andes, *Quat. Sci. Rev.*, *2*, 83-155, 1983.

Corte, A.E., Central Andes rock glaciers: applied aspects, in *Rock Glaciers*, edited by J.R. Giardino, J.F.J. Shroder, and J.D. Vitek, Allen and Unwin, Winchester, Mass., 1987.

Eshleman, V.R., Radar glory from buried craters on icy moons, *Science*, *234*, 587-590, 1986.

Forster, R.R., B.L. Isacks, and S.B. Das, Shuttle Imaging Radar (SIR-C/X-SAR) reveals near-surface properties of the South Patagonian Icefield, *J. Geophys. Res.*, *101*, 23169-23180, 1996.

Freeman, A., M. Alves, B. Chapman, J. Cruz, Y. Kim, S. Shaffer, J. Sun, E. Turner, and K. Sarabandi, SIR-C data quality and calibration results, *IEEE Trans. Geosci. Remote Sens.*, *33*(4), 848-857, 1995.

Gerth, H., *Der Geologische Bau der Sudamerikanischen Kordillere*, Gebr. Borntträger, Berlin, 1955.

Goldstein, R.M., and R.R. Green, Ganymede: radar surface characteristics, *Science*, *207*, 179-180, 1980.

Gurrola, E.M., Interpretation of radar data from icy Galilean satellites and Triton, Ph.D. thesis, Stanford Univ., Stanford, Calif., 1995.

Hagfors, T., Refraction scattering as origin of the anomalous radar returns of Jupiter's satellites, *Nature*, *315*, 637-640, 1985.

Haldemann, A.F.C., Interpreting radar scattering: Circular-polarization perspectives from three terrestrial planets, Ph.D. thesis, Calif. Inst. of Technol., Pasadena, Calif., 1997.

Han, J., T. Zhou, and M. Nakawo, Stratigraphic and structural features of ice cores from Chongce Ice Cap, West Kunlun mountains, *Bull. Glacier Res.*, *7*, 21-29, 1989.

Hapke, B., Coherent backscatter and the radar characteristics of outer planet satellites, *Icarus*, *88*(2), 407-417, 1990.

Hapke, B., and D. Blewitt, Coherent backscatter model for the unusual radar reflectivity of icy satellites, *Nature*, *352*(2), 46-47, 1991.

Harmon, J.K., and M.A. Slade, Radar mapping of Mercury - Full-disk images and polar anomalies, *Science*, *258*(5082), 640-643, 1992.

Harmon, J. K., M. A. Slade, R. A. Velez, A. Crespo, M. J. Dryer, and J. M. Johnson, Radar mapping of Mercury's polar anomalies, *Nature*, *369*, 213-215, 1994.

Holton, J., R., *An Introduction to Dynamic Meteorolgy*, Academic, San Diego, Calif., 1992.

Instituto Geographico Militar (IGM), Sheet "E" 69, 3330-6945, Rio Yeso, Santiago, 1985.

Instituto Geographico Militar (IGM), Sheet "E" 61, 3315-6945, Tupungato, Instituto Geographico Militar, Santiago, 1994.

Jezek, K.C., P. Gogineni, and M. Shanableh, Radar measurements of melt zones on the Greenland Ice Sheet, *Geophys. Res. Lett.*, *21*(1), 33-36, 1994.

Li, C. and P. Cheng, Recent research on glaciers on the Chinghai-Tibet Plateau, *World Glacier Inventory*, *IAHS AISH Publ.*, *126*, 1980.

Li, B., and J. Li, *Quaternary Glacial Distribution Map of the Qinghai-Xizang (Tibet) Plateau*, Science Press, Beijing, 1991.

Lliboutry, L., The origin of penitents, *J. Glaciol.*, *2*, 331-338, 1954.

Lliboutry, L., *Nieves y Glaciares de Chile*, Univ. de Chile, Santiago, 1956.

Lliboutry, L., *Traité de Glaciologie, Glace, Neige, Hydrologie Nivale*, Masson, Paris, 1965a.

Lliboutry, L., *Traité de Glaciologie, Glaciers, Variations du Climat, Sols Gelés*, Masson, Paris, 1965b.

Long, D.G., and M.R. Drinkwater, Greenland Ice-Sheet surface-properties observed by the Seasat-A scatterometer at enhanced resolution, *J. Glaciol.* , *40*(135), 213-230, 1994.

Muhleman, D.O., B.J. Butler, A.W. Grossman, and M.A. Slade, Radar images of Mars, *Science*, *253*(5027), 1508-1513, 1991.

Nakawo, M., Y. Nakayama, T. Kohshima, T. Nishimura, J. Han, and T. Zhou, Ice coring operation at high altitudes in West Kunlun Mountains, China, *Bull. Glacier Res.*, *7*, 15-21, 1989.

Ostro, S.J., Radar properties of Europa, Ganymede, and Callisto, in *Satellites of Jupiter*, edited by D. Morrison, pp. 213-236, Univ. of Arizona Press, Tucson, 1982.

Ostro, S.J., and Pettengill, Icy craters on the Galilean Satellites, *Icarus*, *34*, 268-279, 1978.

Ostro, S.J., et al., Europa, Ganymede, and Callisto: New radar results from Arecibo and Goldstone, *J. Geophys. Res.*, *97*, 18227-18244, 1992.

Paige, D.A., S.E. Wood, and A.R. Vasavada, The thermal-stability of water ice at the poles of Mercury, *Science*, *258*(5082), 643-646, 1992.

Paterson, W.S.B., *The Physics of Glaciers*, Pergamon, Tarrytown, N.Y., 1994.

Peixoto, J.P., and A.H. Oort, *Physics of Climate*, AIP, New York, 1992.

Peters, K. J., Coherent-backscatter effect: A vector formulation accounting for polarization and absorption effects and small or large scatterers, *Phys. Rev. B*, *46*, 801-812, 1992.

Rignot, E., Backscatter model for the unusual radar properties of the Greenland Ice-Sheet, *J. Geophys. Res.*, *100*, 9389-9400, 1995.

Rignot, E.J., S.J. Ostro, J.J. Vanzyl, and K.C. Jezek, Unusual radar echoes from the Greenland Ice Sheet, *Science*, *261*(5129), 1710-1713, 1993.

Rott, H., and R.E. Davis, Multifrequency and polarimetric SAR observations on alpine glaciers, *Ann. Glaciol.*, *17*, 98-104 1993.

Rott, H., and C. Matzler, Possibilities and limits of synthetic aperature radar for snow and glacier surveying, *Ann. Glaciol.*, *9*, 195-200, 1987.

Shih, Y., T. Hsieh, P. Cheng, and C. Li, Distribution, features and variations of glaciers in China, *World Glacier Inventory*, *IAHS AISH Publ.*, *126*, 1980.

Slade, M.A., B.J. Butler, and D.O. Muhleman, Mercury radar imaging - Evidence for polar ice, *Science*, *258*(5082), 635-640, 1992.

Stiles, W.H., and F.T. Ulaby, The active and passive microwave response to snow parameters 1. Wetness, *J. Geophys. Res.*, *85*, 1037-1044, 1980.

Takahashi, S., T. Ohata, and Y. Xie, Characteristics of heat and water fluxes on glacier and ground surfaces in the West Kunlun Mountains, *Bull. Glacier Res.*, *7*, 89-99, 1989.

Thompson, L.G., Climatic changes for the last 2000 years from ice-core evidence in tropical ice cores, in *Climatic Varaitions and Forcing Mechanisms of the Last 2000 Years*, edited by P.D. Jones, pp. 281-295, Springer Verlag, New York, 1996.

Thompson, L.G., E. Mosley-Thompson, M.E. Davis, P.N. Lin, J. Dai, J.F. Bolzan, and T. Yao, A 1000 year ice core record from the Guliya Ice Cap, China: Its relationship to global climate variabilty, *Ann. Glaciol.*, *21*, 175-181, 1995.

Ulaby, F.T., Radar signatures of terrain - Useful monitors of renewable resources, *Proc. IEEE*, *70*(12), 1410-1428, 1982.

Ulaby, F.T., W.H. Stiles, and M. Abdelrazik, Snowcover influence on backscattering from terrain, *IEEE Trans. Geosci. Remote Sens.*, 22(2), 126-133, 1984.

Ulander, L. M. H., Radiometric slope correction of synthetic-aperture radar images, *IEEE Trans. Geosci. Remote Sens.*, *34*, 1115-1122, 1996.

Van Zyl, J.J., B. D. Chapman, P. Dubois, and J. Shi, The effect of topography on SAR calibration, *IEEE Trans. Geosci. Remote Sens.*, *31*, 1036-1043, 1993.

Vitek, J.D., and J.R. Giardino, Rock glaciers: A review, in *Rock Glaciers*, edited by J.R. Giardino, J.F.J. Shroder and J.D. Vitek, Allen and Unwin, Winchester, Mass., 1987.

Watanabe, O. and B. Zheng, First glaciological expedition to West Kunlun Mountains 1985, *Bull. Glacier Res.*, *5*, 77-84, 1987.

Xie, Z., and W. Zhang, Characteristics of ice formation in the West Kunlun Mountains, *Bull. Glacier Res.*, *7*, 29-37, 1989.

Zeil, W., *Geologie von Chile*, Gebr. Bornträger, Berlin, 1964.

Zhang, W., and K. Jiao, Modern glaciers on the south slope of West Kunlun Mountains (in Aksayqin Lake and Guozha Co Lake drainage areas), *Bull. Glacier Res.*, *5*, 85-91, 1987.

Zhang, W., R. An, H. Yang, and K. Jiao, Conditions of glacier development and some glacial features in the West Kunlun Mountains, *Bull. Glacier Res.*, *7*, 49-59, 1989.

Zheng, B., Preliminary studies of Quaternary glaciation and palaeogeography on the south slope of West Kunlun, *Bull. Glacier Res.*, *5*, 93-102, 1987.

Zuhui, S., *Terrain Map of the Qinghai-Xizang Plateau*, Science Press, Shanghai, 1990.

Zwally, H.J., Microwave emissivity and accumulation rate of polar firn, *J. Glaciol.* , *18*, 195-215, 1977.

A. F. C. Haldemann, Jet Propulsion Laboratory, MS 238-420, 4800 Oak Grove Drive, Pasadena, CA 91109-8099. (albert@shannon.jpl.nasa.gov)

D. O. Muhleman, Division of Geological and Planetary Sciences, California Institute of Technology, Pasadena, CA, 91125

(Received November 10, 1997; revised February 26, 1999; accepted March 8, 1999.)